EXCITATION-DEPENDENT NONLINEAR BEHAVIOR OF DISTRIBUTED MICROCRACKS

A Thesis
Presented to
The Academic Faculty

By

Kathrin D. Hoffmann

In Partial Fulfillment
of the Requirements for the Degree
Master of Science in Engineering Science and Mechanics in the
School of Civil and Environmental Engineering

Georgia Institute of Technology

December 2018

EXCITATION-DEPENDENT NONLINEAR BEHAVIOR OF DISTRIBUTED MICROCRACKS

Approved by:

Prof. Laurence J. Jacobs, Advisor
School of Civil and Environmental Engineering
Georgia Institute of Technology

Dr. Jin-Yeon Kim
School of Civil and Environmental Engineering
Georgia Institute of Technology

Prof. Jianmin Qu
Department of Mechanical Engineering
Tufts University

Date Approved: August 22, 2018

ACKNOWLEDGEMENTS

First and foremost, I would like to thank my advisor Professor Laurence J. Jacobs for all his support throughout my whole graduate studies. Without your commitment, neither my studies at Georgia Tech nor this research would have been possible. Also, I highly appreciate the opportunity to participate in the Quantitative Nondestructive Evaluation Conference (QNDE) in Burlington, Vermont.

Furthermore, I would like to thank Dr. Jin-Yeon Kim for his invaluable advice and inspiring ideas, the fruitful discussions, and for sharing his extraordinary experience in research. Thanks also goes to Professor Jianmin Qu for his input and for reviewing this thesis.

I want to thank my labmates Aurelio Bellotti, Brian Fuchs, Sangyun Park and Katie Scott for the great atmosphere in the lab and the trip to QNDE. Special thanks goes to Katie Scott, whose measurements were the starting point of this project, for teaching me the theory and practices in this field.

Moreover, I am very grateful for the support of the Studienstiftung des deutschen Volkes (German Academic Scholarship Foundation) and the Baden-Württemberg Foundation, both financially and immaterially.

Furthermore, I highly appreciate the commitment of Professor Michael Hanss, Dr. Dennis Schurr, Sibylle Langer and Professor Peter Eberhard at the University of Stuttgart in coordinating this unique study abroad program.

Beyond that, I would like to express my gratitude towards my family and friends for all their support.

TABLE OF CONTENTS

LIST OF TABLES

LIST OF FIGURES

LIST OF SYMBOLS AND ABBREVIATIONS

Latin Symbols

A	cross-sectional area
A_n	amplitude of the n-th harmonic wave
$A_{n,2}$	amplitude of the n-th harmonic wave, resulting from the perturbation u_2
a	radius of hemispherical asperities
a_1, a_2, a_3	coefficients in crack volume variation term
$\boldsymbol{b}$	crack opening displacement
b_n	n-th Fourier coefficient
c	crack density $c = NR^3/V$
c_0, c_1	volume fractions of matrix and inclusion
c_L	longitudinal wave velocity
d	distance between middle lines of crack surfaces
d_0	initial distance between middle lines of crack surfaces
$\tilde{d}$	distance variation between crack faces due to wave
E	Young's modulus
$\bar{E}_t, \bar{E}_c, \bar{E}_a$	effective Young's moduli for tension, compression and asperity contact
E_0, E_1	Young's moduli of matrix and inclusion
E_2, E_3	second- and third-order elastic constants
$\boldsymbol{e}_1, \boldsymbol{e}_2, \boldsymbol{e}_3$	basis vectors of the cartesian coordinate system
F	force to compress one asperity
f	frictional force against sliding of crack faces

$f_t, f_{t,\text{shift}}$	derivative terms from the tensile part of $\sigma(\varepsilon)$
$f_c, f_{c,\text{shift}}$	derivative terms from the compressive part of $\sigma(\varepsilon)$
G_1, G_2, G_3	coefficients in the effective stress-strain relationship
g_1, g_2, g_3	functions in the calculation of the strain resulting from cracks
$H[.]$	Heaviside step function
H_1	$H[\varepsilon - \varepsilon_1]$
H_2	$H[\varepsilon - \varepsilon_2]$
h	height of asperities
h_s	$\sqrt{2}$ times effective height of roughness
k	wave number
K_0, K_1	bulk moduli of matrix and inclusion
k_F, k_σ	crack stiffness parameters in spring model
$\boldsymbol{n}$	surface normal vector
N	number of cracks
N_0	crack concentration $N_0 = N/V$
p	absolute value of the external load
$\boldsymbol{q}$	traction at the crack faces
R	crack radius
$\boldsymbol{s}$	direction of shear stress in the crack plane
S	crack surface
T	period
t	time
u	displacement
u_1	primary displacement solution
u_2	secondary displacement solution
V	volume
$W(h)$	top height distribution function

x	cartesian coordinate
$\boldsymbol{x}$	position vector
Y	argument $\omega t - kx$ of displacement solution
Y_i	parameter depending on transition between crack states
	$Y_i = \arccos(-\varepsilon_i/(kA_1)), \quad i = 1, 2$

Greek Symbols

β	acoustic nonlinearity parameter
β_B	acoustic nonlinearity parameter, defined differently in bilinear stiffness model
β_{RSC}	acoustic nonlinearity parameter, from parameters of rough surface contact model
$\gamma_{1,t}, \gamma_{1,c}$	relative change in Young's modulus with reference E
γ_t, γ_c	relative change in Young's modulus with reference $\bar{E}_c$
ΔV	crack volume variation
δ	displacement of asperities
$\delta[.]$	Dirac delta function
δ_1	$\delta[\varepsilon - \varepsilon_1]$
δ_2	$\delta[\varepsilon - \varepsilon_2]$
ε	strain
ε_1	strain at which the crack closes completely
ε_2	strain at which the crack opens up completely
$\hat{\boldsymbol{\varepsilon}}^*$	strain field from one crack
$\boldsymbol{\varepsilon}^*$	strain field from all cracks
$\bar{\boldsymbol{\varepsilon}}^*$	volume average strain from all cracks
$\bar{\boldsymbol{\varepsilon}}_0$	strain from external stress
θ	angle between crack normal and $\boldsymbol{e}_2$-axis
λ	wavelength
μ	shear modulus

ν	Poisson's ratio
ρ	density
σ	normal stress
σ_0	normal stress to press crack faces together
σ_1	normal stress from compression of asperities
σ_i	initial stress
$\tilde{\sigma}$	stress due to wave
τ	shear stress at crack faces
φ	angle between crack normal and $\boldsymbol{e}_3$-axis
$\psi(\boldsymbol{n})$	crack orientation distribution function
ω	circular frequency

Abbreviations

COD	crack opening displacement
NDE	nondestructive evaluation
NFA	nanostructured ferritic alloy
RSC	rough surface contact
SHG	second harmonic generation

SUMMARY

It is well known that microcracks generate strong higher harmonics in propagating monochromatic waves. There is a large amount of literature on modeling this phenomenon, but most of these existing papers only describe one specific mechanism. For example, Zhao et al. [36] assumes that the crack faces are either open under tension or closed under compression, and in the latter case they may slide against each other. On the other hand, the Nazarov and Sutin [23] model assumes microcracks as an elastic contact of two rough surfaces, which are never completely separated by an external load. All these mechanisms depend on the level of excitation.

In this research, a micromechanical model for the acoustic nonlinearity generation of microcracks is developed by combining the bilinear stiffness model and the rough surface contact model to describe the excitation-dependent nonlinear behavior of distributed microcracks. It is shown that the first and second harmonic amplitudes have the relationship: $A_2 \sim A_1^n$, with n dependent on the amplitude of excitation, and $2 \geq n \geq 1$ for non-adhesive crack surfaces.

Nanostructured ferritic alloys (NFA) [26] are considered as an example. These materials exhibit outstanding high-temperature properties, irradiation tolerance and thermal stability, making them a leading candidate for advanced nuclear fission and fusion applications. One characteristic property of mechanically processed NFAs is their layer-like structure, with a large number of microcracks aligned in a specific direction. Nonlinear ultrasound measurements (acoustic nonlinearity, β) with longitudinal waves are used to characterize this material. The results show that these measurement techniques are sensitive to the orientation of the cracks. The model developed in this research is then used to interpret these experimental measurements and used to characterize the microcracks in a NFA specimen.

CHAPTER 1
INTRODUCTION AND BACKGROUND

1.1 Motivation

Nonlinear ultrasound provides a powerful method to characterize the microstructure of materials. This is particularly useful for nondestructive evaluation (NDE) applications, which aim to detect material damage at an early stage. NDE has great potential to determine the damage state of critical components, especially in applications where high safety standards have to be met, such as the energy, transportation and construction industries. In these fields, despite aging infrastructure, safe and effective operation has to be guaranteed. NDE techniques do not only secure the structural integrity of safety-critical parts, but can also reduce maintenance costs.

1.1.1 Nonlinear Ultrasound and Second Harmonic Generation Techniques

Nonlinear ultrasound has the advantage over linear ultrasound in that it is sensitive to microstructural features which are orders of magnitude smaller than the wavelength [21]. For this reason, microscopic damage can be detected before macroscopic cracks form and grow to a critical size. Second harmonic generation (SHG) measurement techniques are a subset of nonlinear ultrasonic NDE techniques, which were first developed and applied in the 1960s. In these measurements, the interaction of a propagating monochromatic elastic wave with the material's microstructure generates a second harmonic wave. Microstructural features that cause such nonlinearity, are, for example, dislocations, precipitates and microcracks. Therefore, microstructural changes, which occur during the service of a material, due to fatigue, thermal aging, creep and radiation damage, can be detected and characterized with SHG. The nonlinearity is quantified in terms of the acoustic nonlinearity

parameter β. A comprehensive overview of SHG theory, microstructural contributions to the nonlinearity parameter, and experimental techniques is given in [21].

1.1.2 Micromechanics Models

This research focuses on solids which contain microscopic cracks. These cracks can be caused by fatigue damage, stress-corrosion cracking, or, as is the case in the material considered in this thesis, by delamination along grain boundaries. Microcracks lead to a nonlinear stress-strain-relationship that generates higher harmonics in propagating monochromatic waves. The interactions between acoustic waves and microcracks have to be understood and described mathematically in order to nondestructively evaluate the damage in a microcracked material with ultrasonic methods. To this end, it is necessary to investigate the relationship between the acoustic nonlinearity parameter β and the parameters of the cracked solid, such as crack density.

1.1.3 Application: Nanostructured Ferritic Alloys (NFA)

The derivations in this thesis are carried out for microcracks that lie in planes parallel to each other. This applies to materials with a layer-like structure, e.g. from mechanical processing, which leads to microcracks that are aligned in a specific direction. As an example, nanostructured ferritic alloys (NFAs), which show this structure, are considered. These alloys are currently being developed, and the recent progress in the field as well as material properties are reported by Odette et al. [26], [25] and Kim et al. [17]. Their papers are briefly summarized in the following.

These new materials are iron-chromium-based ferritic stainless steels containing a very high concentration of Y-Ti-O rich nano-oxides. The nano-oxide features give rise to the following properties: First, they retard dislocation climb and glide and, therefore, increase the alloy's strength. Second, they stabilize the grain and dislocation structures. Third, they trap helium from radiation influence, so that small high-pressure gas bubbles form at

the interface between the nano-oxide and the matrix. This mechanism controls the transport of helium and enhances stabilization and recombination. Additionally, the material is characterized by small grain sizes and high dislocation densities. Therefore, NFAs feature multiple high-performance properties. They have high tensile strength (600 to 1600 MPa, depending on the heat treatment), creep and fatigue strength over a wide range of temperatures. They show thermal stability up to 1000°C. Moreover, they are able to tolerate irradiation, particularly the high concentration of helium being present, very well.

These properties make NFAs a leading candidate for advanced nuclear fission and fusion applications. In that field, the structural integrity of materials is crucial. Therefore, possible damage mechanisms in the material have to be understood. Mechanically processed NFAs, typically by rolling, are highly anisotropic and consist of layered particles. Consequently, the most brittle and least stiff direction is perpendicular to the layers. The microstructure, cracks and delaminations are depicted schematically in figure 1.1. Figure 1.2 is a scanning electron microscope image of the corresponding delamination cracks. The figure shows that the cracks are parallel to each other and can be modeled as penny-shaped, which will be applied in this thesis.

Measurements performed on the NFA specimen [30] show a significant 67 % difference in the acoustic nonlinearity parameter between wave propagation parallel to the aligned cracks and perpendicular to them. This demonstrates that nonlinear ultrasound is sensitive to the orientation of the cracks.

1.2 Literature Review

There is a large amount of literature on modeling the influence of microcracks on the mechanical behavior, particularly estimating the effective moduli of cracked solids; see Mura's fundamental reference [22] for an overview. To describe the interactions between ultrasonic waves and microcracks, there are various models of crack-induced nonlinearities, which

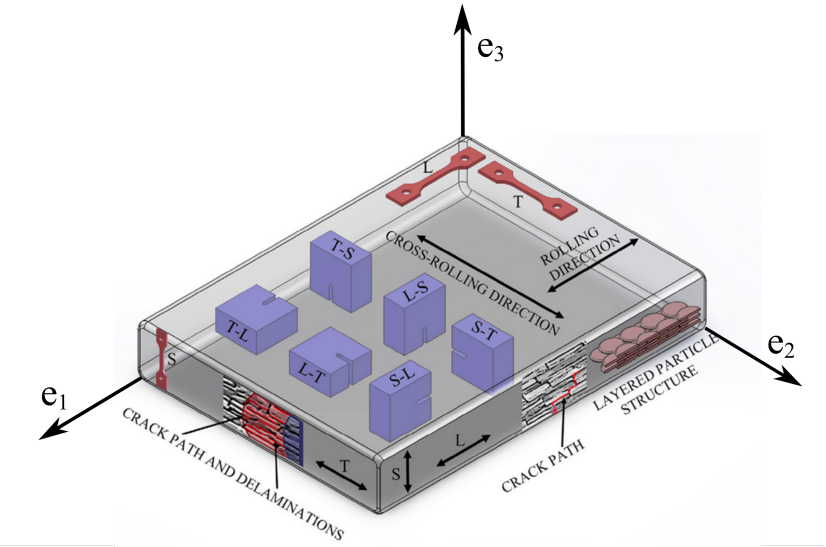

Figure 1.1: Schematic orientation and microstructure of NFA [26].

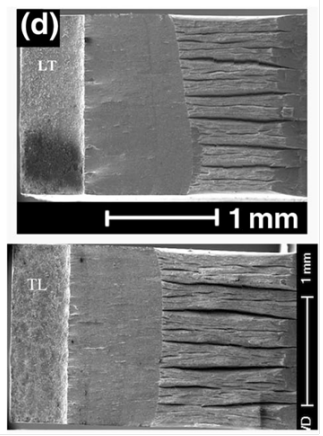

Figure 1.2: Scanning electron microscope image of microcracks in NFA specimen [26].

were recently reviewed by Broda et al. [2]. There are three major concepts: The bilinear stiffness model, the rough surface contact model and the hysteresis model. The bilinear stiffness model assumes that the crack faces are open under tension and closed under compression, so that the effective elastic properties are different in each case, which induces acoustic nonlinearity. In the rough surface contact model, the crack faces consist of many irregularities, which deform in a nonlinear manner when subjected to a propagating wave, thus causing acoustic nonlinearity. In the hysteresis model, the stress-strain relationship contains a hysteresis loop, which leads to acoustic nonlinearity, and, additionally, energy

dissipation, as for instance described by Guyer and Johnson [12].

In this thesis, the bilinear stiffness model and rough surface contact model will be used.

1.2.1 Models Based on Bilinear Stiffness

A fundamental explicit derivation of the effective elastic properties of bodies containing randomly distributed penny-shaped cracks, based on the Eshelby method and a self-consistent scheme, was presented by Budiansky and O'Connell in 1976 [5]. The authors assume that the cracks remain open all the time, which corresponds to the states of solids under external tensile loading. The Young's modulus of the cracked solid under tension is smaller than that of an identical solid without cracks, because the cracks are open, which reduces the overall stiffness. Horii and Nemat-Nasser [13] include the fact that some cracks may be closed and undergo frictional sliding. This approach describes a load-induced anisotropy, where moduli depend on the loading conditions and the loading path [13],[16]. Various concepts to calculate the effective elastic properties of cracked solids were critically reviewed by Kachanov [15]. In more recent research, Zhao et al. [36] derived the acoustic nonlinearity parameter that results from such tension and compression asymmetry.

1.2.2 Models Based on Rough Surface Contact (RSC)

Alternatively, many authors have focused on wave interaction with interfaces and rough surfaces, and they have modeled cracks as such a contact. An early experimental study, published by Buck et al. in 1978 [4], shows that higher harmonics are generated at unbonded interfaces and fatigue cracks. In 1979, in the corresponding theoretical investigation, Richardson [28] formulated the nonlinear dynamics of a system consisting of an unbonded planar interface separating two semi-infinite linear elastic media. This phenomenon is called contact acoustic nonlinearity and is directly related to the nonlinearity generation from crack interfaces. Another mechanism of contact acoustic nonlinearity is the so-called

clapping motion of crack faces, for example examined by Solodov [33].

Nazarov and Sutin (1997) [23] apply methods from elastic contact mechanics to cracks with rough surfaces, pressed together under internal stresses from the surrounding solid. They utilize this crack model to derive the acoustic nonlinearity parameter β for elastic solids with randomly distributed penny-shaped cracks, so that β is related to the properties of the contacting rough crack faces. Cantrell [7] uses and re-formulates the Nazarov and Sutin model to point out the acoustic nonlinearity generation from such a microcrack model.

Moreover, Cantrell [6] shows that the total number of cracks in a material, described by Nazarov and Sutin's model, generates a much higher nonlinearity than the total number of dislocation substructures resulting from fatigue.

In the field of contact mechanics, in 1966 Greenwood and Williamson presented a fundamental model for the contact of nominally flat surfaces [11]. It describes a purely elastic deformation of asperities, with heights quantified by a probability density function. Both Nazarov / Sutin's and Greenwood / Williamson's models are based on the Hertz solution for the pressure distribution in the contact between a hemisphere and a rigid surface, which will be used in this thesis, as well. The theory of elastic contact mechanics, which is incorporated in both models, is explained, for example, in [14]. Using such a contact mechanics approach in finite element simulations, Oberhardt [24] models the microcracks by an effective stress-strain relationship and calculates the acoustic nonlinearity.

In their recent paper, Rjelka et al. [29] apply finite element simulations to penny-shaped flat cracks and cracks with a Hertzian contact. They find that these two types of cracks contribute differently to the acoustic nonlinearity of the overall cracked solid.

1.3 Objective

It is well known that microcracks generate strong higher harmonics in propagating monochromatic waves. As seen in the literature review, most of the existing papers on this phe-

nomenon describe only one specific mechanism: either the opening / closing of cracks and sliding of crack faces or the rough surface contact. However, these mechanisms are present at the same time, depending on the level of excitation.

The overall goal of this research is to develop a micromechanical model for the acoustic nonlinearity generation of microcracks, in order to describe the excitation-dependent nonlinear behavior of distributed microcracks. To this end, the bilinear stiffness model and the rough surface contact model are combined to obtain the overall effective elastic properties of cracked solids.

1.4 Outline

In chapter 2, the fundamentals of linear and nonlinear wave propagation will be explained. Chapter 3 introduces the bilinear stiffness model and the RSC model for microcracked materials and additionally a general calculation scheme from micromechanics. In chapter 4, for each model a more detailed derivation is carried out and simulation results are presented, followed by an overall stress-strain relationship that combines both models. Chapter 5 focuses on the nonlinear wave equation, using the constitutive equations from the previous chapter, to compute the amplitudes of the first, second and higher harmonics and to analyze their relationship. Chapter 6 outlines the experimental procedure and results. Chapter 7 draws a conclusion and gives an outlook to possible future work.

CHAPTER 2

WAVE PROPAGATION

This thesis deals with time-harmonic plane longitudinal waves in elastic solids. A wave is called time-harmonic (also named monochromatic), if it has one constant circular frequency ω. In a plane wave, per definition, the displacement varies only in the propagation direction, i.e. the wave fronts are parallel. In longitudinal waves, which are the subject of this research, the amplitude vector is parallel to the propagation direction. In this work, dissipation, scattering and diffraction effects are not taken into account.

2.1 Linear Wave Propagation

In order to derive the governing equation of a one-dimensional longitudinal wave, consider a thin, homogeneous rod of density ρ. This and the following section are based on the procedure in Graff's book [10]. An infinitesimal volume element $\mathrm{d}V$ of length $\mathrm{d}x$ is shown in figure 2.1. Let the x-axis be the longitudinal axis of the rod, and displacements along this axis are named $u(x,t)$. The rod is subjected to a longitudinal stress field $\sigma(x,t)$, varying with time t, but constant over the cross-section A.

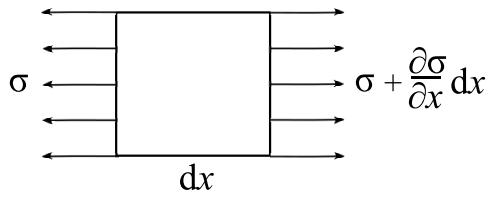

Figure 2.1: Infinitesimal volume element of a rod subjected to a longitudinal stress.

The equation of motion for the infinitesimal volume element in the x-direction, in the

absence of body forces, reads

$$\rho A \, \mathrm{d}x \frac{\partial^2 u}{\partial t^2} = -\sigma A + \big(\sigma + \frac{\partial \sigma}{\partial x} \, \mathrm{d}x\big) A. \tag{2.1}$$

This leads to the governing equation of a longitudinal wave propagating through an isotropic solid

$$\rho \frac{\partial^2 u}{\partial t^2} = \frac{\partial \sigma}{\partial x}. \tag{2.2}$$

For a linear elastic solid the constitutive equation is

$$\sigma = E\varepsilon = E \frac{\partial u}{\partial x}. \tag{2.3}$$

It is assumed that the material is homogeneous, so that its properties E and ρ are constant. Plugging (2.3) into (2.2), the wave equation becomes

$$\rho \frac{\partial^2 u}{\partial t^2} = \frac{\partial}{\partial x}\Big(E \frac{\partial u}{\partial x}\Big). \tag{2.4}$$

Rearranging and introducing the longitudinal wave velocity (also: phase velocity) $c_L = \sqrt{E/\rho}$ yields

$$\frac{\partial^2 u}{\partial t^2} = c_L^2 \frac{\partial^2 u}{\partial x^2}. \tag{2.5}$$

The solution to this partial differential equation is the displacement wave

$$u = A \sin(\omega(\tfrac{x}{c_L} - t)), \tag{2.6}$$

where A is the amplitude and ω the circular frequency. For convenience, the solution to the wave equation is often expressed in terms of complex functions

$$u = A e^{i\omega(\frac{x}{c_L} - t)} = A\big(\cos(\omega(\tfrac{x}{c_L} - t)) + i \sin(\omega(\tfrac{x}{c_L} - t))\big) \tag{2.7}$$

and it is implied that the physical displacement components are the real or imaginary parts of this expression [1].

The physical quantity $k = \frac{\omega}{c_L}$ is called the wave number. It is related to the period T by $\omega = 2\pi/T$ and to the wavelength λ by $k = 2\pi/\lambda$. Hence, the solution for the displacement of a plane wave can be rewritten as

$$u = Ae^{i(kx-\omega t)} = A\big(\cos(kx-\omega t) + i\sin(kx-\omega t)\big). \tag{2.8}$$

In a three-dimensional coordinate system, a plane harmonic wave propagating in the direction defined by the unit vector $\boldsymbol{p}$ is described by

$$\boldsymbol{u} = \boldsymbol{A}e^{ik(\boldsymbol{x}\cdot\boldsymbol{p}-c_L t)}. \tag{2.9}$$

2.2 Nonlinear Wave Propagation

In the previous section, it was assumed that the material's behavior is linear, i.e. that after an excitation with circular frequency ω only waves of the same frequency ω occur in the material. If the constitutive equations of the medium are nonlinear, however, higher harmonic waves are generated. The frequencies of these waves are integer multiples of the fundamental frequency with which the medium was excited. Figure 2.2 shows a schematic of the linear and nonlinear cases.

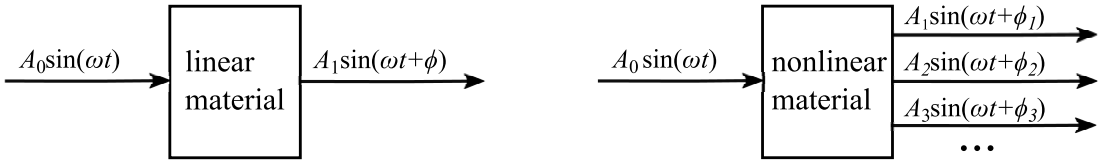

Figure 2.2: Wave propagation in linear and nonlinear material.

The nonlinearity of the material can for instance be caused by cracks, as described in chapter 1. The following explanation is based on [10] and [21]. For quadratic nonlinearity,

the constitutive equation becomes

$$\sigma = \sigma_i + E_2 \frac{\partial u}{\partial x} + \frac{1}{2} E_3 \Big(\frac{\partial u}{\partial x} \Big)^2, \tag{2.10}$$

where σ_i is the initial stress in the material and E_2 and E_3 are the second and third order elastic constants of the material.

Plugging equation (2.10) into the general equation of motion (2.2) leads to the nonlinear wave equation for longitudinal waves

$$\frac{\partial^2 u}{\partial t^2} = c_L^2 \Big(1 - \beta \frac{\partial u}{\partial x} \Big) \frac{\partial^2 u}{\partial x^2}. \tag{2.11}$$

The quantity β is called the nonlinearity parameter. According to the derivation of equation (2.11), β is related to the elastic constants in equation (2.10) by

$$\beta = -\frac{E_3}{E_2}. \tag{2.12}$$

Unlike the linear case, the time-harmonic solution to the nonlinear wave equation (2.11) also contains higher harmonics of circular frequencies $2\omega, 3\omega$ etc. and is of the form

$$u = A_1 \sin\big(\omega\big(\frac{x}{c_L} - t\big)\big) + \frac{\beta A_1^2 x \omega}{8 c_L} \cos\big(2\omega\big(\frac{x}{c_L} - t\big)\big) + \cdots . \tag{2.13}$$

The first harmonic has the amplitude A_1 and the second harmonic the amplitude

$$A_2 = \frac{\beta A_1^2 x \omega^2}{8 c_L^2}. \tag{2.14}$$

Based on this expression for A_2, the acoustic nonlinearity parameter β is defined as

$$\beta = \frac{8 c_L^2 A_2}{A_1^2 \omega^2 x}, \tag{2.15}$$

i.e. it is proportional to A_2/A_1^2. This means that in order to determine the acoustic nonlinearity parameter experimentally, the amplitudes of the first and second harmonic waves, the propagation distance, circular frequency and wave velocity have to be measured. When a second harmonic wave is generated in the material, there is energy transferred from the first to the second harmonic. However, the energy loss of the first harmonic is often neglected in the literature due to the following reasons: First, the amplitude A_2 is several decades smaller than the amplitude A_1. Second, for small propagation distances x, the energy decrease of A_1 is much smaller than the total energy of the first harmonic wave.

The derivation of β can be extended and adapted to the three-dimensional case as well as to special types of waves.

CHAPTER 3

GENERAL MODELING APPROACHES FOR MICROCRACKED MATERIALS

This chapter provides an introduction to the mathematical modeling of microcracks and their effect on the acoustic nonlinearity parameter β.

When a wave propagates through the microcrack, three different states can occur: Under large tensile stresses, the cracks are open. With large compressive stresses being present, the cracks are completely closed. In the case of small tensile or compressive stresses, the asperities of the rough crack faces are in contact, and the crack is neither completely open or completely closed.

In this thesis, the bilinear stiffness model [35], [36] and rough surface contact (RSC) model [7],[23] are incorporated. The tensile part of the bilinear stiffness model, which refers to open cracks, is applied for sufficiently large values of tensile stresses. For large absolute values of compressive stresses, the closed cracks are described by the compressive part of the bilinear stiffness model. The RSC model is used for asperity contact in the case of small tensile or compressive stresses.

Each of the two modeling approaches bilinear stiffness model and RSC model consists of three steps: First, a micromechanical model of the crack is formulated, which is different in both approaches. The second step uses this crack model to calculate the effective stress-strain relationship of the cracked solid. In both models, the overall strain results from linear superposition of the strain from the external stress applied to the uncracked solid, and the additional strain that is caused by the crack and described in the respective crack model. Third, the effective stress-strain relationship is inserted into the wave equation, so that the amplitudes of the first and second harmonics, and subsequently the acoustic nonlinearity parameter β can be determined.

It has to be pointed out that different authors define different mechanisms as the source

of nonlinearity. In the bilinear stiffness model, the tension-compression asymmetry introduces nonlinearity [35]. In contrast, in the RSC model, the elastic deformation of asperities gives rise to acoustic nonlinearity [7]. This will be shown in more detail in the following sections.

A crack is called a microcrack if its size is "much smaller than all other characteristic lengths of interest, such as the size of the representative volume element (RVE) or the wavelength" [36]. For both models, the following assumptions are made, which are common for quantifying the effects of microcracks in solids:

– The uncracked solid is linear, so that acoustic nonlinearity results only from the nonlinear behavior of the microcracks. This is valid when the acoustic nonlinearity from the cracks is much higher than that of the uncracked solid, which has been shown in many papers, such as [4], [32].

– The total strain in a cracked medium is the sum of the strain in the solid without cracks and the additional strain that results from the cracks. Moreover, the stress is uniform and the stress applied to each of the cracks is equal to the external stress applied to the whole solid [23], [36].

– The crack density is assumed to be low, so that crack interactions can be neglected. This so-called dilute concentration estimate has a wide range of applicability, as shown by Kachanov [15], who points out that even for higher crack densities, stress shielding and amplification cancel out. Under this assumption, the strain field due to all cracks is the sum of the individual strain fields from each crack.

– The crack radius is small compared to the overall medium. This defines a microcrack, whereas for macrocracks other methods are used. In the NFA material modeled in this thesis, microscopic images show that the crack radius is approximately 1 mm, whereas the dimensions of the specimen are multiple centimeters. Usually, microcracks are even smaller, so that this assumption is justified.

– The cracks are uniformly distributed [15]. In the NFA material modeled in this thesis,

microscopic images show a layer-like regular structure that confirms the uniform distribution.

Both crack models that are introduced in this thesis deal with microcracks which have the following properties: The cracks are assumed to be penny-shaped with radius R. Let the solid contain N cracks per volume V. In their model, Zhao et al. [36] use the crack density parameter $c = NR^3/V$. It represents the combined effect of the crack size and the number of cracks per unit volume. In Nazarov and Sutin's model, the crack concentration is defined purely volumetrically as $N_0 = N/V$ (number of cracks per volume).

Figure 3.1 shows the general three-dimensional coordinate system that will be used in this thesis. The orientation of each crack is defined by its unit normal vector $\boldsymbol{n} = \sin(\varphi)\cos(\theta)\boldsymbol{e}_1 + \sin(\varphi)\sin(\theta)\boldsymbol{e}_2 + \cos(\varphi)\boldsymbol{e}_3$, which is constant on each crack surface. The angles lie in the ranges $0 \leq \varphi \leq \pi/2,\ 0 \leq \theta \leq 2\pi$.

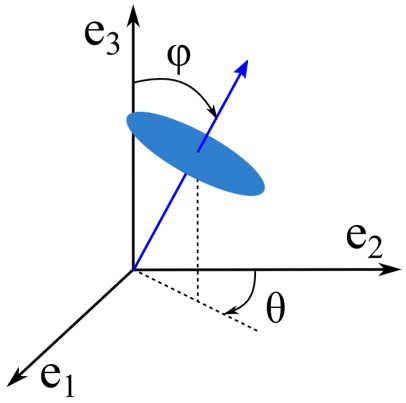

Figure 3.1: Coordinate system for crack orientation.

3.1 Bilinear Stiffness Model (Opening-Closing Model)

Let the uncracked solid have Young's modulus E and Poisson's ratio ν. In the bilinear stiffness model, also called opening-closing model, the crack is open under tension and closed under compression. Therefore, the effective tensile and compressive moduli of the

solid are different. Closed cracks may additionally undergo frictional sliding of the crack faces.

In this section, the procedure to calculate the effective Young's moduli $\bar{E}_i$ with indices $\mathrm{i} = \mathrm{t}$ for tension and $\mathrm{i} = \mathrm{c}$ for compression will be summarized for randomly oriented cracks, based on [36]. Additionally, the authors of [36] take into account that the effective moduli are frequency-dependent under dynamic loading. However, this effect will be neglected in this thesis, which is a usual assumption in the literature on the bilinear stiffness model. Moreover, in simulations the frequency-dependency was found to be small.

Since this research focuses on a longitudinal wave propagating along the principal axes of the material, which leads to uniaxial loading conditions, the elastic properties $\bar{E}_i$ and $\bar{\nu}_i$ are sufficient to describe the linear elastic behavior of the material. In chapter 4, the effective moduli will be re-derived in more detail for aligned microcracks.

If a general surface traction is applied to the solid, this leads to the following traction $\boldsymbol{q}$ at the crack faces

$$\boldsymbol{q} = \sigma_{\mathrm{n}}\boldsymbol{n} + (\tau + f)H[\tau + f]\boldsymbol{s} \tag{3.1}$$

σ_{n} : normal stress

τ : shear stress

f : frictional force against sliding of crack faces

$H[.]$: Heaviside step function

$\boldsymbol{n}$: surface normal vector

$\boldsymbol{s}$: direction of shear stress in the crack plane,

in which the tangential component $\tau + f$ is only active if the shear stress is larger than the frictional force that resists the sliding of crack faces.

The crack opening displacement (COD) is defined as $\boldsymbol{b}(\boldsymbol{x}) \equiv \boldsymbol{u}(\boldsymbol{x})|_{\boldsymbol{x}\epsilon S^+} - \boldsymbol{u}(\boldsymbol{x})|_{\boldsymbol{x}\epsilon S^-}$,

where $S^{\pm}$ are the two crack surfaces. The strain corresponding to this COD is

$$\hat{\boldsymbol{\varepsilon}}^{*}(\boldsymbol{n},\boldsymbol{x}) = \tfrac{1}{2}(\boldsymbol{b}\otimes\boldsymbol{n} + \boldsymbol{n}\otimes\boldsymbol{b})\delta_S[S-\boldsymbol{x}] \tag{3.2}$$

[27], where $\otimes$ is the outer (dyadic) product and $\delta_S[S-\boldsymbol{x}] = \int_S \delta[\boldsymbol{z}-\boldsymbol{x}]\,\mathrm{d}S(\boldsymbol{z})$ is the surface Dirac delta function, which leads to a local integration over the crack.

Under the dilute concentration approximation, the strain field $\boldsymbol{\varepsilon}^{*}$ from all cracks results from integrating over the strain fields of each individual crack

$$\boldsymbol{\varepsilon}^{*} \equiv \int_D \hat{\boldsymbol{\varepsilon}}^{*}(\boldsymbol{n},\boldsymbol{x})\psi(\boldsymbol{n})\,\mathrm{d}\Omega(\boldsymbol{n}) \tag{3.3}$$

$\psi(\boldsymbol{n})$: crack orientation distribution function

$\mathrm{d}\Omega(\boldsymbol{n}) = \sin\varphi\,\mathrm{d}\theta\,\mathrm{d}\varphi$: solid angle element

$D \equiv \{\theta,\varphi : 0\le\theta\le 2\pi,\ 0\le\varphi\le\pi/2\}$: domain of integration.

Making use of the superposition principle, the average strain in the volume V is the sum of the strain $\bar{\boldsymbol{\varepsilon}}_0$ induced by the external stress, and the volume average strain $\bar{\boldsymbol{\varepsilon}}^{*}$ due to the cracks

$$\bar{\boldsymbol{\varepsilon}} = \bar{\boldsymbol{\varepsilon}}_0 + \bar{\boldsymbol{\varepsilon}}^{*} = \bar{\boldsymbol{\varepsilon}}_0 + \frac{1}{V}\int_V \boldsymbol{\varepsilon}^{*}(\boldsymbol{x})\,\mathrm{d}V(\boldsymbol{x}). \tag{3.4}$$

More detailed expressions for the above equations will be given for the case of aligned microcracks in chapter 4. For the general derivation, see [36]. In the case of randomly oriented cracks, the orientation distribution function is $\psi(\boldsymbol{n}) = N/(2\pi)$.

In the next step, a uniaxial load p in the $\mathbf{e}_3$ direction is applied and static tensile and compressive loading are considered separately.

This load causes the strain $\bar{\boldsymbol{\varepsilon}}_0 = \frac{p}{E}\big(-\nu(\boldsymbol{e}_1\otimes\boldsymbol{e}_1 + \boldsymbol{e}_2\otimes\boldsymbol{e}_2) + \mathbf{e}_3\otimes\mathbf{e}_3\big)$ in the absence of cracks. In the presence of cracks, an expression with the same structure is expected, but

with the effective moduli $\bar{E}_i, \bar{\nu}_i$ instead of E and ν:

$$\bar{\boldsymbol{\varepsilon}} = \frac{p}{\bar{E}_i}\big(- \bar{\nu}_i(\boldsymbol{e}_1 \otimes \boldsymbol{e}_1 + \boldsymbol{e}_2 \otimes \boldsymbol{e}_2) + \mathbf{e}_3 \otimes \mathbf{e}_3\big). \tag{3.5}$$

In order to compute $\bar{\boldsymbol{\varepsilon}}$, the above integrals have to be carried out. The procedure is explained in [36] and leads in the tensile case to

$$\bar{\boldsymbol{\varepsilon}}^* = \frac{16pc}{45E}\,\frac{1-\nu^2}{2-\nu}\big(- \nu(\boldsymbol{e}_1 \otimes \boldsymbol{e}_1 + \boldsymbol{e}_2 \otimes \boldsymbol{e}_2) + (10-3\nu)\mathbf{e}_3 \otimes \mathbf{e}_3\big). \tag{3.6}$$

Comparison to equation (3.5) yields the coefficients $\bar{E}_t$ and $\bar{\nu}_t$. Therefore, the effective properties of an elastic solid containing randomly oriented penny-shaped microcracks are in the tensile case

$$\frac{\bar{E}_t}{E} = \frac{45(2-\nu)}{45(2-\nu) + 16(1-\nu^2)(10-3\nu)c} \tag{3.7}$$

$$\frac{\bar{\nu}_t}{\nu} = \frac{45(2-\nu) + 16(1-\nu^2)c}{45(2-\nu) + 16(1-\nu^2)(10-3\nu)c}\,, \tag{3.8}$$

which has been derived by numerous authors, see also [20]. A similar procedure for the compressive case results in

$$\frac{\bar{E}_c}{E} = \frac{45(2-\nu)}{45(2-\nu) + 64F_1(1-\nu^2)c} \tag{3.9}$$

$$\frac{\bar{\nu}_c}{\nu} = \frac{45(2-\nu)\nu + 32F_1(1-\nu^2)c}{45(2-\nu) + 64F_1(1-\nu^2)(10-3\nu)c}\,, \tag{3.10}$$

where F_1 depends on the coefficient of friction between the possibly sliding crack faces. For the coefficient of friction $\mu = 0$ it is $F_1 = 1$ and for $\mu \to \infty,\ F_1$ goes to zero.

Once the effective moduli in the bilinear stiffness model are known, the next step is to calculate the acoustic nonlinearity that results from such tension-compression asymmetry. The computation procedure is outlined in [35] and will be summarized in the following.

For simplicity, the calculation is performed for a uniaxial strain $\varepsilon = \partial u/\partial x$ in the x-direction of a cracked medium, with u being the displacement in this direction. Since the cracked solid has a bilinear stiffness, its Young's modulus is rewritten using the terms

$$\gamma_{1,t} = \frac{E - \bar{E}_t}{E}, \qquad \gamma_{1,c} = \frac{E - \bar{E}_c}{E}, \tag{3.11}$$

which denote the relative change in E. Zhao et al. [36] have shown that $\gamma_{1,t} \ll 1,\ \gamma_{1,c} \ll 1$ even for high crack densities. Herewith, the overall Young's modulus becomes

$$E_o = E\Big(1 - \gamma_{1,t} H\Big[\frac{\partial u}{\partial x}\Big] - \gamma_{1,c} H\Big[-\frac{\partial u}{\partial x}\Big]\Big), \tag{3.12}$$

where $H[.]$ is the Heaviside step function. Then the normal stress in the x-direction of the cracked solid is $\sigma = E_o \frac{\partial u}{\partial x}$. Inserting this stress-strain relationship into the wave equation (2.2) yields

$$\frac{\partial^2 u}{\partial t^2} - c_L^2 \frac{\partial^2 u}{\partial x^2} = -\gamma_{1,t} c_L^2 H\Big[\frac{\partial u}{\partial x}\Big] \frac{\partial^2 u}{\partial x^2} - \gamma_{1,c} c_L^2 H\Big[-\frac{\partial u}{\partial x}\Big] \frac{\partial^2 u}{\partial x^2} \tag{3.13}$$

where $c_L = \sqrt{E/\rho}$ is the longitudinal wave velocity. The terms on the right-hand side result from

$$\frac{\partial}{\partial x}\Big(H\Big[\frac{\partial u}{\partial x}\Big] \frac{\partial u}{\partial x}\Big) = H\Big[\frac{\partial u}{\partial x}\Big] \frac{\partial^2 u}{\partial x^2}, \tag{3.14}$$

using $\frac{\partial}{\partial x} H[x] = \delta[x]$ with the Dirac delta function and its property $x\delta[x] = 0$. The physical interpretation of the right-hand side of 3.13 is that the system nonlinearity is caused by the deviation of $\bar{E}_t$ and $\bar{E}_c$ from E of the uncracked solid.

By solving the above boundary-value problem (3.13) using a perturbation method, and taking the Fourier transform of the solution, Zhao et al. [35] find the amplitude of the second harmonic to be

$$A_2 = \frac{(\gamma_{1,t} - \gamma_{1,c}) A_1 x \omega}{3\pi c_L}. \tag{3.15}$$

Significant about this result is that A_2 is proportional to A_1, whereas for uncracked solids A_2 is proportional to A_1^2. Therefore, [35] defines the acoustic nonlinearity parameter β_B of cracked solids in the bilinear stiffness model as

$$\beta_B \equiv \frac{3\pi c_L A_2}{A_1 \omega x}. \tag{3.16}$$

This result is different from the usual definition for uncracked solids, where $\beta \equiv (8c_L^2 A_2)/(A_1^2 \omega^2 x)$ [21].

Inserting equation (3.15) into the definition (3.16) yields

$$\beta = \gamma_{1,t} - \gamma_{1,c}, \tag{3.17}$$

which indicates that the nonlinearity parameter is proportional to the tension-compression asymmetry in the elastic modulus. Recall that the quantities $\gamma_{1,i}$ are expressed in terms of the effective moduli $\bar{E}_i$ and the latter are known functions of the crack density c.

3.2 Rough Surface Contact (RSC) Model

Nazarov and Sutin model a crack as the elastic contact of two initially rough surfaces that are pressed together by the internal stress from the surrounding material [23]. When no wave propagates through the material, the two crack surfaces are in a static equilibrium. With an incident longitudinal wave being present, this inherent normal contact stress at the interface is superimposed by the normal stress that results from the wave.

For their crack model, Nazarov and Sutin use an elastic contact mechanics approach. Typical assumptions that were introduced in Greenwood and Williamson's rough surface contact model [11] and are used in [23] as well as in most of the literature are:

– The rough surface is isotropic.

– The asperity tops are elastic hemispheres with equal radii a and heights h according to the distribution function $W(h)$. In this assumption, the rough surface contact relates back

to classical contact mechanics theory, e.g. from Johnson's book [14].

– There is no bulk deformation when the asperities are in contact, and only the hemispheres are deformed. Moreover, the asperities are so far apart that interactions between them can be neglected.

– Only normal stresses act on the crack and change its volume. Shear stresses are neglected. Since in the measurement on the NFA material all cracks are perpendicular to the incident wave, it is justified to take only normal stresses into account.

Figure 3.2 shows this modeling approach for a single crack, which is described in this section. The rough surface contact is depicted in the top subfigure. The stresses in the elastic contact depend only on the profiles of the two surfaces relative to each other. Therefore, the main idea is to replace the two contacting surfaces by an equivalent contact between a plane rigid surface and an elastic solid that combines the profiles of the two rough surfaces. The latter is characterized by initially undeformed asperities, twice as high as those of a single rough surface. The middle subfigure shows the equivalent contact. With this setup, a standard contact mechanics approach as in [14] can be worked out, which is outlined in the following. As a reference, a middle line of the profile is defined. The rough surface is parameterized in terms of a height distribution function $W(h)$, which describes the number of asperity tops that have height h from the middle line. This function is normalized per crack surface area. Consequently, $W(h)\,\mathrm{d}h$ is the number of tops with a height from h to $h + \mathrm{d}h$ per crack surface area. This setup is depicted in the bottom subfigure.

When the two surfaces are pressed together, the asperities deform. More specifically, given a distance d between the middle lines of the two surfaces, it follows that all tops being initially higher than d are deformed and become flattened. In this case, where $h > d$, the displacement of an asperity is defined as $\delta = h - d$.

The force that is required to compress one top by an approach δ depends on the shape of the asperity. Nazarov and Sutin [23] assume that there are three possible shapes of the asperity: A part of a sphere, an obtuse cone, or a cylinder. According to [11], in

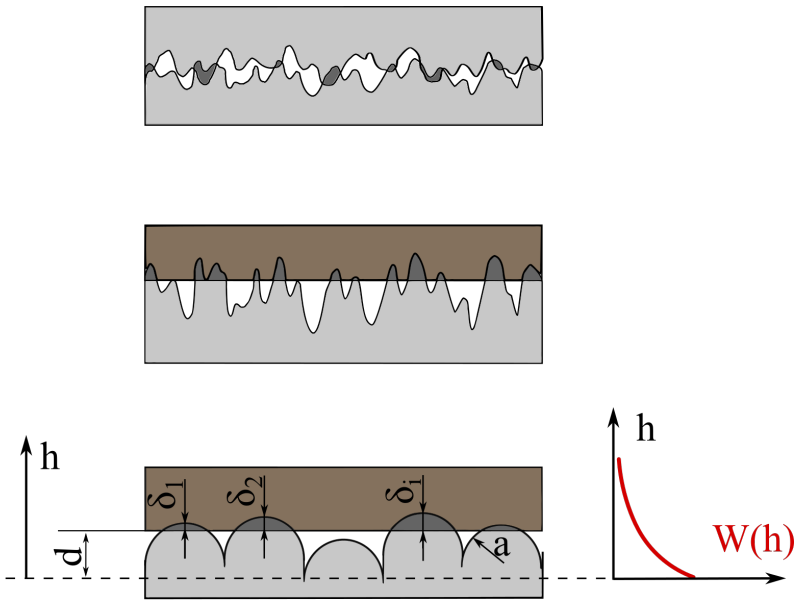

Figure 3.2: Modeling the rough surface contact. Top: original contact between two surfaces, middle: equivalent contact between rigid plane and effective roughness, bottom: modeling asperities as hemispheres with statistical distribution of top heights.

this work, the asperities are modeled as hemispheres with radius a. Figure 3.2 shows the deformation of the equivalent contact with spherical asperities. The behavior of each asperity is described by the Hertzian equations [14], [34]. In particular, the force F required to compress one spherical asperity by an approach δ is

$$F = \frac{4}{3}\frac{E}{2(1-\nu^2)}\sqrt{\frac{a}{2}}\sqrt{\delta^3}. \tag{3.18}$$

In order to calculate the total stress resulting from the compression of the irregularities in the contact area, the integral over the forces for all tops with $h \geq d$ has to be carried out:

$$\sigma_1(d) = -\int_d^\infty F(h-d)W(h)\,\mathrm{d}h. \tag{3.19}$$

The calculation is performed in chapter 4 for spherical irregularities and an exponential height distribution functions.

Physically, the stress σ_1 tries to open up the crack. Nazarov and Sutin point out that if

the crack is in an equilibrium state, this stress σ_1 has to be compensated by a stress σ_0 of equal magnitude but opposite sign. Physically, σ_0 is the internal stress in the surrounding uncracked solid. The equilibrium state of the crack is characterized by

$$\sigma_0 = \sigma_1. \tag{3.20}$$

In their model, [23] focus on the relationship between the crack geometry and the local stress on the crack. One basic equation in their approach is the relationship between the external stress σ_0 applied to the crack with plane surfaces and the crack volume V_0,

$$\sigma_0 = \frac{3EV_0}{16R^3(1-\nu^2)}. \tag{3.21}$$

It is assumed that this relationship determines the internal stress σ_0 to press the crack faces together. Let the crack with plane surfaces have the volume $V_0 = \pi R^2 d_0$, where d_0 is the initial distance between the middle lines of the crack faces. By inserting the expression for V_0 in (3.21), the stress σ_0 in terms of the crack opening d_0 is

$$\sigma_0(d_0) = \frac{3\pi E d_0}{16R(1-\nu^2)} \tag{3.22}$$

If a wave propagates through the crack, there is an additional acoustic stress $\tilde{\sigma}$ present in the crack, which leads to a crack surface distance variation $\tilde{d}$. Then the dynamic equilibrium becomes

$$\tilde{\sigma} = \sigma_0(d_0 + \tilde{d}) - \sigma_1(d_0 + \tilde{d}), \tag{3.23}$$

which gives an explicit relationship between $\tilde{\sigma}$ and $\tilde{d}$.

Depending on the underlying height distribution $W(h)$ it is more or less straight-forward to invert this relationship in order to calculate the distance variation $\tilde{d}$ from the measurable stress variation $\tilde{\sigma}$, which will be carried out in chapter 4. Then, the overall idea is to plug the relationship between crack geometry and stress from the crack model into more general

stress-strain relations that determine the acoustic parameters of a cracked medium.

3.3 Micromechanical Averaging Schemes

A solid that contains cracks is a heterogeneous material. In the field of micromechanics, there are multiple methods to approximately determine the effective moduli of such materials. The most common approaches are based on the Eshelby solution for an ellipsoidal inclusion in a solid, which is a fundamental result in micromechanics. The derivation of such averaging schemes to calculate effective properties can be found in [22] and [27], and in this section their results are outlined briefly.

Consider an elastic solid that consists of a matrix, in the following having the index "0", that contains ellipsoidal inhomogeneities, having the index "1". The volume fraction of inhomogeneities is c_1, then the volume fraction of the matrix phase is $c_0 = 1 - c_1$. Let c_1 be sufficiently small, $c_1 \ll 1$, so that interactions between inhomogeneities can be neglected and dilute concentration estimates are valid [22]. The averaging schemes Eshelby method and Mori-Tanaka method have straight-forward analytical solutions, thus requiring the least computational effort. Unlike the Eshelby method, the Mori-Tanaka method yields the correct limit for $c_1 \to 1$ [27]. This means that, while the Eshelby method is only valid for the low-concentration limit, the Mori-Tanaka method is more accurate for higher volume fractions of inclusions. Therefore, the Mori-Tanaka method is preferred in this work.

In this scheme, the effective bulk modulus $\bar{K}$ and the effective shear modulus $\bar{\mu}$ of an inhomogeneous material are determined by

$$\bar{K} = K_0 + \frac{c_1(K_1 - K_0)(3K_0 + 4\mu_0)}{3K_0 + 4\mu_0 + 3(1 - c_1)(K_1 - K_0)} \tag{3.24}$$

$$\bar{\mu} = \mu_0 + \frac{5c_1\mu_0(\mu_1 - \mu_0)(3K_0 + 4\mu_0)}{5\mu_0(3K_0 + 4\mu_0) + 6(1 - c_1)(\mu_1 - \mu_0)(K_0 + 2\mu_0)} \tag{3.25}$$

[27], using $K_i = E_i/\big(3(1 - 2\nu_i)\big)$, $\mu_i = E_i/(2(1 + \nu_i))$. Then, the effective Young's

modulus and Poisson's ratio become

$$\bar{E} = \frac{9\bar{K}\bar{\mu}}{3\bar{K} + \bar{\mu}} \tag{3.26}$$

$$\bar{\nu} = \frac{3\bar{K} - 2\bar{\mu}}{6\bar{K} + 2\bar{\mu}}. \tag{3.27}$$

CHAPTER 4

NONLINEAR ELASTIC PROPERTIES OF THE CRACKED SOLID

In this chapter, the two modeling approaches bilinear stiffness model and RSC model for the effective properties of the microcracked material are carried out. Then, the two models, which only describe one specific mechanism, are combined into a more comprehensive model. All the derivations are formulated for aligned microcracks, i.e. all have the same normal vector, for two reasons: First, if only normal stresses act on the crack, purely the opening-closing motion and RSC occur. With all cracks being perpendicular to the wave, the stress vector does not have to be decomposed into its normal and shear components and there are no shear stresses and, therefore, no frictional sliding. As a consequence, the physical meaning of the developed model becomes more clear. Second, in the NFA [26] to which the models will later be applied in this thesis, all microcracks are aligned. The solid with aligned penny-shaped cracks is transversely isotropic, whereas uniformly distributed crack orientations lead to material isotropy. The case of randomly oriented microcracks can easily be covered by using the crack orientation distribution function $\psi(\boldsymbol{n}) = N/(2\pi)$ instead of the Dirac delta function for one specific orientation. Consequently, an integration over all orientations is required, so that most equations in the model contain one integral more for randomly oriented cracks. Moreover, the assumptions stated in chapter 3 are presumed in this chapter, too.

In the subsequent sections, the different models will be derived. Each derivation is followed by a numerical example for the NFA modeled in an exemplary way in this thesis. The numerical values used are listed in table 4.1. The parameters R, N_0 and d_0 are estimated using microscopic images from [26]. These values lie in the same range as the ones used for estimations in the RSC model paper [23]. The asperity radius a is chosen such that the stiffness of the cone approximately equals the value that [23] use for their conical

Table 4.1: Material and wave parameters.

symbol	value	explanation
E	190 GPa	Young's modulus of uncracked material [26]
ν	0.25	Poisson's ratio of uncracked material [23]
R	$0.5 \cdot 10^{-3}$ m	crack radius [26]
N_0	$3 \cdot 10^{8}$	number of cracks per m^3 [23]
h_S	10^{-8} m	$\sqrt{2}$ times effective height of roughness
a	$2 \cdot 10^{-4}$ m	radius of conical asperity
d_0	$3 \cdot 10^{-8}$ m	initial distance between crack faces [26]
x	$8.509 \cdot 10^{-3}$ m	thickness of specimen [30]
ω	$1.319 \cdot 10^{8}$	circular frequency, corresponds to $f = 21$ MHz [30]
c	5972 m/s	longitudinal wave velocity [30]

asperities. The crack density parameter $c = NR^3/V$ in the bilinear stiffness model follows from the purely volumetric crack density $N_0 = N/V$ in the RSC model and the crack radius and is $c = 0.0375$. This is a low crack density, for which the dilute concentration estimate is appropriate.

Parameterizing such a model is usually one of the biggest challenges in material modeling. Images from scanning electron microscopy can be used to determine parameters of the rough surface. In their paper, Greenwood and Williamson [11] did not only provide a theoretical model on RSC, but also an experimental study of the surface topography. Numerical examples on parameterizing probability density functions as well as experimental results were, for example, performed by Brown and Scholz [3].

4.1 Bilinear Stiffness Model

Following the procedure of [36], the effective elastic properties of a microcracked solid will be computed, using the bilinear stiffness model. This is carried out for aligned microcracks, i.e. the orientation of all cracks is described by the same unit normal vector, here $\boldsymbol{n} = \boldsymbol{e_3}$. In this case, the crack orientation distribution function becomes $\psi = N\delta[\varphi]$.

4.1.1 Derivation

In this section, the effective Young's modulus will be derived, based on the procedure summarized in chapter 3.

The additional strain (3.3) induced by the cracks becomes

$$\boldsymbol{\varepsilon}^* = \hat{\boldsymbol{\varepsilon}}^*(\boldsymbol{e}_3, \boldsymbol{x})N, \tag{4.1}$$

where

$$\hat{\boldsymbol{\varepsilon}}^*(\boldsymbol{e}_3, \boldsymbol{x}) = \tfrac{1}{2}(\boldsymbol{b} \otimes \boldsymbol{e}_3 + \boldsymbol{e}_3 \otimes \boldsymbol{b})\delta_S[S - \boldsymbol{x}]. \tag{4.2}$$

The volume average strain from the cracks is

$$\bar{\boldsymbol{\varepsilon}}^* = \frac{1}{V}\int_V \boldsymbol{\varepsilon}^*(\boldsymbol{x})\,\mathrm{d}V(\boldsymbol{x}). \tag{4.3}$$

Using the property $\int_V f(\boldsymbol{x})\delta_S[S - \boldsymbol{x}]\,\mathrm{d}V(\boldsymbol{x}) = \int_S f(\boldsymbol{x})\,\mathrm{d}S(\boldsymbol{x})$ of the surface Dirac delta function, this becomes

$$\bar{\boldsymbol{\varepsilon}}^*(\boldsymbol{e}_3, \boldsymbol{x}) = \frac{N}{2V}\int_S (\boldsymbol{b} \otimes \boldsymbol{e}_3 + \boldsymbol{e}_3 \otimes \boldsymbol{b})\,\mathrm{d}S(\boldsymbol{x}). \tag{4.4}$$

As $\boldsymbol{n} = \boldsymbol{e}_3$ is constant over the whole crack surface, the integral is rewritten as

$$\int_S \big(\boldsymbol{b}\,\mathrm{d}S(\boldsymbol{x})\big) \otimes \boldsymbol{e}_3 + \boldsymbol{e}_3 \otimes \big(\int_S \boldsymbol{b}\,\mathrm{d}S(\boldsymbol{x})\big). \tag{4.5}$$

For penny-shaped cracks, [36] gives the COD $\boldsymbol{b}(\boldsymbol{x})$ and carries out the integral, which defines the crack opening volume. In the case of aliged microcracks, the crack opening

volume is

$$\boldsymbol{v} \equiv \int_S \boldsymbol{b}(\boldsymbol{x})\,\mathrm{d}S(\boldsymbol{x}) \tag{4.6}$$

$$= \frac{16R^3(1-\nu^2)}{3E}\big(\sigma_{\mathrm{n}}H[\sigma_{\mathrm{n}}]\boldsymbol{n} + \frac{2}{2-\nu}(\tau+f)H[\tau+f]\boldsymbol{s}\big) = \text{const.}. \tag{4.7}$$

Thus, equation (4.3) becomes

$$\bar{\boldsymbol{\varepsilon}}^* = \frac{16NR^3(1-\nu^2)}{3EV}\big(\sigma_{\mathrm{n}}H[\sigma_{\mathrm{n}}]\boldsymbol{n}\otimes\boldsymbol{n} + \frac{2}{2-\nu}(\tau+f)H[\tau+f](\boldsymbol{s}\otimes\boldsymbol{n}+\boldsymbol{n}\otimes\boldsymbol{s})\big). \tag{4.8}$$

Let a longitudinal wave propagate through the cracked solid, with propagation direction perpendicular to the cracks, so that it causes only normal tractions at the crack faces. There is no shear stress and no frictional sliding of the crack faces, and the direction $\boldsymbol{s}$ of the shear stress is undefined. Under a uniaxial tensile load p in the $\boldsymbol{e}_3$ direction, it follows that

$$\bar{\boldsymbol{\varepsilon}}^* = \frac{16c(1-\nu^2)p}{3E}\big(\sigma_{\mathrm{n}}H[\sigma_{\mathrm{n}}]\boldsymbol{e}_3\otimes\boldsymbol{e}_3\big), \tag{4.9}$$

where the crack density $c = NR^3/V$ is plugged in.

From superposition, the overall strain in the cracked solid is

$$\begin{aligned}\bar{\boldsymbol{\varepsilon}} &= \bar{\boldsymbol{\varepsilon}}_0 + \bar{\boldsymbol{\varepsilon}}^* \\ &= \frac{p}{E}\big(-\nu(\mathbf{e}_1\otimes\mathbf{e}_1+\mathbf{e}_2\otimes\mathbf{e}_2)+\mathbf{e}_3\otimes\mathbf{e}_3\big) + \frac{p}{E}\Big(\frac{16c(1-\nu^2)}{3}\mathbf{e}_3\otimes\mathbf{e}_3\Big) \\ &= \frac{p}{\bar{E}_t}\big(-\bar{\nu}_t(\boldsymbol{e}_1\otimes\boldsymbol{e}_1+\boldsymbol{e}_2\otimes\boldsymbol{e}_2)+\mathbf{e}_3\otimes\mathbf{e}_3\big).\end{aligned} \tag{4.10}$$

Comparing coefficients yields the effective elastic properties in the tensile case

$$\bar{E}_t = \frac{E}{1+\frac{16}{3}c(1-\nu^2)} \tag{4.11}$$

$$\bar{\nu}_t = \nu. \tag{4.12}$$

The resulting effective moduli are interpreted physically as follows: Under tensile loading, the cracks are completely open in the bilinear stiffness model, which reduces the stiffness of the solid. Since no shear or friction occur, the material behavior in the transverse direction remains the same, so that Poisson's ratio does not change.

In the case of a compressive external load p normal to the cracks, it follows from equation (4.3) that $\bar{\boldsymbol{\varepsilon}}^* = 0$, and, thus, $\bar{\boldsymbol{\varepsilon}} = \bar{\boldsymbol{\varepsilon}}_0$. Consequently, the effective compressive moduli are

$$\bar{E}_c = E \tag{4.13}$$

$$\bar{\nu}_c = \nu. \tag{4.14}$$

As outlined in chapter 3, equations (3.11) and (3.17) then yield the acoustic nonlinearity parameter β.

4.1.2 Simulation

Figure 4.1 shows the effective tensile modulus as a function of crack density. A crack density of 0.2 is a high value and corresponds, for example, to 200 cracks of radius 1 mm in 1 cm^3 of the solid. For this crack density, the Young's modulus in the cracked material is 35% lower than in the uncracked. Under compressive loading, the cracks are completely closed in the bilinear stiffness model, so that they have no influence on the elastic properties. Therefore, E remains unchanged. The bilinear stress-strain relationship for the crack density $c = 0.0375$ in the specimen is depicted in figure 4.2. The solid line is the stress-strain curve with slope E of the uncracked solid, and the dashed line represents the reduced stiffness of the cracked solid under tension.

Since under stresses purely normal to the crack, both shear and friction are zero, the properties in the transverse direction remain unchanged in this model. Consequently, Poisson's ratio stays the same as in the uncracked material for both tensile and compressive

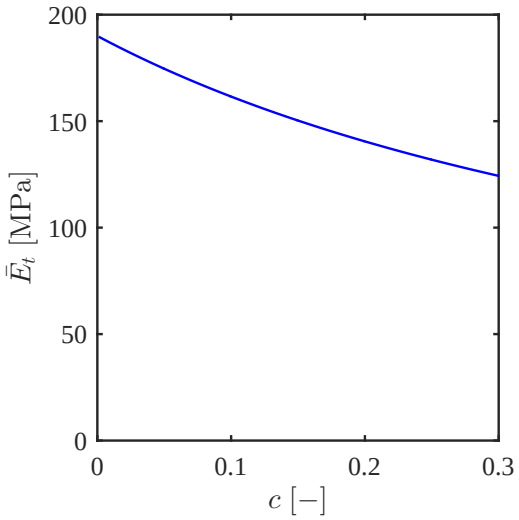

Figure 4.1: Effective tensile Young's modulus $\bar{E}_t$ in bilinear stiffness model as a function of crack density c.

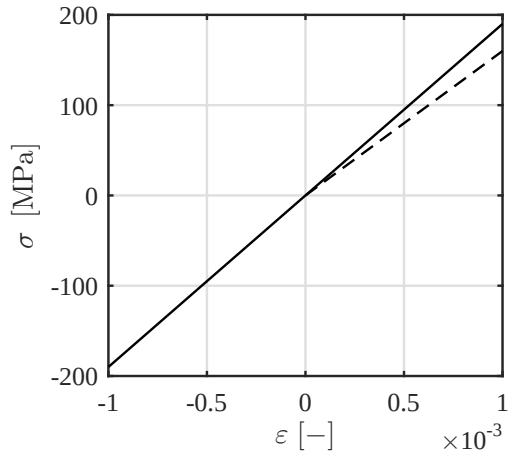

Figure 4.2: Solid: linear stress-strain relationship of the uncracked material. Dashed: bilinear stress-strain relationship for material with crack density $c = 0.0375$, leading to a reduced tensile stiffness $\bar{E}_t$.

external loading.

If a load is applied in the $\boldsymbol{e}_1$ or $\boldsymbol{e}_2$ direction instead, the derivation yields $\bar{E}_i = E$ and $\bar{\nu}_i = \nu$. This occurs because a normal stress in the plane of the crack does neither apply normal nor shear stresses to the crack faces and all terms introduced in this model drop. More general loading cases are covered by equation (4.8).

In the next step, the acoustic nonlinearity parameter β is calculated from equation (3.17). Figure 4.3 shows its dependency on the crack density. Since the relative change in E is small, also β has values smaller than one.

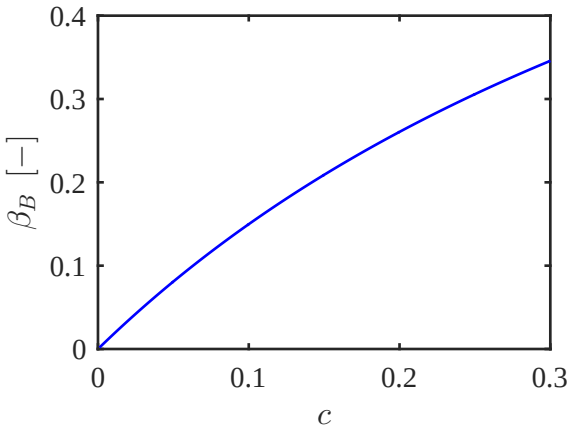

Figure 4.3: Acoustic nonlinearity in bilinear stiffness model as a function of crack density.

4.2 Rough Surface Contact (RSC) Model

Similar to the idea in the previous section, the RSC model assumes that the overall strain is the sum of the strain from the external stress and some additional strain from the cracks.

4.2.1 Derivation

In this section, the model by Nazarov and Sutin [23] is adapted and extended for a solid with aligned cracks. Nevertheless, for the sake of completeness this derivation is started for randomly oriented cracks as in [23] and later specified for aligned cracks. Consider a thin rod under uniaxial stress σ along its longitudinal axis, which is set as the $\boldsymbol{e_3}$ axis. In

the uncracked solid, this leads to a longitudinal strain $\varepsilon_{33} = \sigma/E$ and transverse strains $\varepsilon_{11} = \varepsilon_{22} = -\nu\sigma/E$.

To describe the crack orientation, the same coordinate system from figure 3.1 as in the previous section is used. Based on this geometry, a single crack at an angle φ to the $\boldsymbol{e_3}$ axis is subjected to the normal stress $\sigma_\mathrm{n} = \sigma\cos(\varphi)^2$. As in the previous section, the crack distribution $\psi(\varphi, \theta)$ is specified as a function of φ and θ per unit volume and per unit solid angle. Multiplying this function with the solid angle element $\sin(\varphi)\,\mathrm{d}\varphi\,\mathrm{d}\theta$ gives the number of cracks per unit volume whose normals have orientations from φ to $\varphi + \mathrm{d}\varphi$ and θ to $\theta + \mathrm{d}\theta$.

An incident longitudinal wave produces a variation in the volume of a single crack $\Delta V(\varphi)$. This effect leads to the additional strain

$$\mathrm{d}\varepsilon_{33} = \Delta V(\varphi)\cos(\varphi)^2\psi_0(\varphi,\theta)\sin(\varphi)\,\mathrm{d}\varphi\,\mathrm{d}\theta. \tag{4.15}$$

The additional strain due to all cracks in the material results from an integration over the angles φ and θ. Beyond that, the total strain is computed as the sum of the strain from the external load and the strain due to the cracks:

$$\varepsilon_{33} = \frac{\sigma}{E}\big(1 + \int_0^{2\pi}\int_0^{\pi/2}\psi(\varphi,\theta)\Delta V\cos(\varphi)^2\sin(\varphi)\,\mathrm{d}\varphi\,\mathrm{d}\theta\big). \tag{4.16}$$

The volume change ΔV, which has been introduced in the above equations, will be calculated from the model of a single crack in a separate step. The main idea of [23] is, to relate the crack volume variation to the normal stress σ_n acting on the crack. This dependence is formulated as a general nonlinear function $\Delta V = f(\sigma_\mathrm{n}/E)$ in terms of the normal strain σ_n/E and expanded in the Taylor series

$$\Delta V = a_1\Big(\frac{\sigma_\mathrm{n}}{E}\Big) + \frac{a_2}{2}\Big(\frac{\sigma_\mathrm{n}}{E}\Big)^2 + \frac{a_3}{6}\Big(\frac{\sigma_\mathrm{n}}{E}\Big)^3 + \cdots. \tag{4.17}$$

The coefficients a_1, a_2 and a_3 will then be determined from the microcrack model summarized in section 3.2. It is assumed that stresses are small, $\sigma \ll E$. Plugging (4.17) into (4.16), the resulting equation is rewritten as

$$\varepsilon = \frac{\sigma}{E}(1 + g_1 + \frac{\sigma}{E}g_2 + \frac{\sigma^2}{E^2}g_3) \tag{4.18}$$

where

$$g_1 = a_1 \int_0^{2\pi} \int_0^{\pi/2} \psi(\varphi, \theta) \cos(\varphi)^4 \sin(\varphi) \, \mathrm{d}\varphi \, \mathrm{d}\theta \tag{4.19a}$$

$$g_2 = \frac{a_2}{2} \int_0^{2\pi} \int_0^{\pi/2} \psi(\varphi, \theta) \cos(\varphi)^6 \sin(\varphi) \, \mathrm{d}\varphi \, \mathrm{d}\theta \tag{4.19b}$$

$$g_3 = \frac{a_3}{6} \int_0^{2\pi} \int_0^{\pi/2} \psi(\varphi, \theta) \cos(\varphi)^8 \sin(\varphi) \, \mathrm{d}\varphi \, \mathrm{d}\theta. \tag{4.19c}$$

In the case of aligned cracks in planes parallel to the $\boldsymbol{e_1 e_2}$ plane, the crack orientation function simplifies to a Dirac delta function $N_0 \delta[\varphi]$ with N_0 being the cracks per volume. Consequently, the integral over the orientations drops. Then, it is obtained that

$$g_1 = a_1 N_0 \tag{4.20a}$$

$$g_2 = \frac{a_2}{2} N_0 \tag{4.20b}$$

$$g_3 = \frac{a_3}{6} N_0. \tag{4.20c}$$

Nazarov and Sutin calculate the inverse relationship $\sigma(\varepsilon)$ from (4.18) under the assumptions $\sigma/E \ll 14/(a_2 N_0 G_1)$ and $\sigma/E \ll 27 a_2/(7 a_3)$. This leads to

$$\sigma(\varepsilon) = E G_1 \Big(\varepsilon - \frac{G_2}{2}\varepsilon^2 - \frac{G_3}{6}\varepsilon^3 \Big) \tag{4.21}$$

where

$$G_1 = \frac{1}{1+g_1} \quad \overset{\text{aligned}}{=} \quad \frac{1}{1+N_0 a_1} \tag{4.22a}$$

$$G_2 = \frac{2g_2}{(1+g_1)^2} \quad \overset{\text{aligned}}{=} \quad \frac{N_0 a_2}{(1+N_0 a_1)^2} \tag{4.22b}$$

$$G_3 = \frac{6g_3\big(1-\frac{2g_2^2}{g_3(1+g_1)}\big)}{(1+g_1)^3} \quad \overset{\text{aligned}}{=} \quad N_0 a_3 \frac{1}{(N_0 a_1+1)^3}\Big(\frac{-3N_0 a_2^2}{a_3(N_0 a_1+1)}+1\Big) \tag{4.22c}$$

Comparison with equation (2.10) shows that the coefficients G_i in Nazarov and Sutin's model are related to the elastic constants E_i by $E_2 = EG_1$ and $E_3 = -EG_1G_2$. It was shown in chapter 2 that plugging the nonlinear constitutive equation (2.10) into the wave equation leads to the general expression $\beta = -E_3/E_2$ for the acoustic nonlinearity parameter. More particularly, for the RSC model, this yields the acoustic nonlinearity parameter $\beta = G_2$. It relates the amplitudes of the first and second harmonics by $\beta = (8c_L^2 A_2)/(A_1^2\omega^2 x)$, as derived in chapter 2. Since G_2, quantifying the acoustic nonlinearity from the RSC model, is of particular interest for this research, the written-out expression is

$$G_2 = \frac{N_0 R^4 h_s (16\nu^2-16)^2}{9d_0^2\pi\big(\frac{N_0R^3h_s(16\nu^2-16)}{3d_0(h_s/d_0+1)}-1\big)^2\big(h_s/d_0+1\big)^3} \equiv \beta_{\mathrm{RSC}}. \tag{4.23}$$

This quantity will be called β_{RSC} in the following to distinguish it from the acoustic nonlinearity parameter β_B in the bilinear stiffness model, which was defined differently.

The term G_1 is

$$G_1 = -\Big(\frac{N_0 h_s(16\nu^2-16)R^3}{3d_0(h_s/d_0+1)}-1\Big)^{-1}. \tag{4.24}$$

Next, the crack model, introduced in section 3.2 to determine the required crack parameters will be carried out and examined in more detail.

In this thesis, an exponential distribution function of irregularity heights is chosen for the following two reasons: First, it is a special case of the general χ^2 distribution function.

Consequently, the statistical theory developed in the literature, such as [18], is applicable. Second, the exponential function can conveniently be integrated, and, thus, the calculations can be performed analytically [23]. This is particularly advantageous for the subsequent steps, in which the equations have to be manipulated in various ways. The exponential top height distribution is specified by

$$W(h) = \frac{n}{\pi R^2 h_s} \exp\left(\frac{-h}{h_s}\right) \tag{4.25}$$

n : number of tops on the crack surface

$h_s = \sqrt{2}\, h_0$: with h_0 being the effective height of the roughness.

With this height distribution function, the stress σ_1 in equation (3.19), resulting from integration, is

$$\sigma_1(d) = -nM_1 \exp\left(\frac{d}{h_s}\right). \tag{4.26}$$

The parameter M_1 depends on the geometry of the asperities and is for spherical tops

$$M_1 = \frac{1}{\sqrt{2\pi} R^2} E^* \sqrt{a} \sqrt{h_s^3}, \tag{4.27}$$

where $E^* = E/(2 - 2\nu^2)$ [23].

In the static equilibrium defined by Nazarov and Sutin with no wave being present, the absolute values of σ_0 and σ_1 are equal:

$$\sigma_0(d_0) = \frac{3\pi E d_0}{16 R(1-\nu^2)} = nM_1 \exp\left(\frac{d_0}{h_s}\right) = -\sigma_1(d_0). \tag{4.28}$$

This relationship provides two equations for the three unknowns d_0, σ_0 and n, so that there is only one independent parameter. If, firstly, the number of irregularities n on the crack surface is measured, this determines the static distance between the middle lines and

the static stress that presses the crack faces together. Secondly, specifying the distance d_0 between the crack faces implies values for σ_0 and n. This approach is chosen in this research, as d_0 can be obtained from microscopic images. Thirdly, although it is a physical quantity, the stress σ_0 cannot be measured.

If a wave propagates through the crack, the static equilibrium becomes distorted and the dynamic equilibrium (3.23) holds [23]. In the case of an exponential height distribution it reads

$$\begin{aligned}\tilde{\sigma} &= \frac{3\pi E}{16R(1-\nu^2)}(d_0+\tilde{d}) - nE_1 \exp\Big(-\frac{d_0+\tilde{d}}{h_s}\Big) \\ &= \sigma_0 + \frac{3\pi E}{16R(1-\nu^2)}(\tilde{d}) - \sigma_0 \exp\Big(\frac{-\tilde{d}}{h_s}\Big).\end{aligned} \tag{4.29}$$

Applying a Taylor series expansion to the term with the exponential yields

$$\sigma_0 \exp\Big(\frac{-\tilde{d}}{h_s}\Big) = \sigma_0\big(1 - \frac{\tilde{d}}{h_s} + \frac{1}{2}\Big(\frac{\tilde{d}}{h_s}\Big)^2 - \frac{1}{6}\Big(\frac{\tilde{d}}{h_s}\Big)^3 \pm \cdots\big), \tag{4.30}$$

so that the relationship between the acoustic stress and the distance variation becomes

$$\frac{\tilde{\sigma}}{\sigma_0} = 1 + \frac{h_s}{d_0}\Big(\frac{\tilde{d}}{h_s}\Big) - \frac{1}{2}\Big(\frac{\tilde{d}}{h_s}\Big)^2 + \frac{1}{6}\Big(\frac{\tilde{d}}{h_s}\Big)^3 \pm \cdots . \tag{4.31}$$

In their paper, Nazarov and Sutin make the assumption that the acoustic stress and respective distance variation are small, $|\tilde{\sigma}| \ll \sigma_0$, $|\tilde{d}| \ll d_0$. If additionally the small distance variation fulfills $\tilde{d}/h_s \ll 2(1+h_s/d_0)$, they invert the relationship to obtain $\tilde{d}$ and conclude

$$\Delta V = \pi R^2 \tilde{d} = \pi R^2 h_s \left(\frac{1}{1+\frac{h_s}{d_0}}\Big(\frac{\tilde{\sigma}}{\sigma_0}\Big) + \frac{1}{2}\frac{1}{(1+\frac{h_s}{d_0})^3}\Big(\frac{\tilde{\sigma}}{\sigma_0}\Big)^2 + \frac{1}{6}\frac{2-\frac{h_s}{d_0}}{(1+\frac{h_s}{d_0})^4}\Big(\frac{\tilde{\sigma}}{\sigma_0}\Big)^3 \right) \tag{4.32}$$

This equation is of the same form as equation (4.17), where the additional stress due to the wave $\tilde{\sigma}$ corresponds to the normal stress σ_{n}. Therefore, the microcrack model provides the

required parameters a_1, a_2, a_3, which are

$$a_1 = \pi h_s^2 \Big(\frac{E}{\sigma_0}\Big) \frac{1}{1 + \frac{h_s}{d_0}} \tag{4.33a}$$

$$a_2 = \pi h_s^2 \Big(\frac{E}{\sigma_0}\Big)^2 \frac{1}{(1 + \frac{h_s}{d_0})^3} \tag{4.33b}$$

$$a_1 = \pi h_s^2 \Big(\frac{E}{\sigma_0}\Big)^3 \frac{2 - \frac{h_s}{d_0}}{(1 + \frac{h_s}{d_0})^4}, \tag{4.33c}$$

cf. [23]. Using these parameters, the volume change and, consequently, the overall stress-strain relationship of the cracked solid are parameterized. Note that the stress σ_0 to press the crack faces together does not explicitly enter the overall stress-strain relationship, but is indirectly included in the coefficients.

4.2.2 Simulation

In this subsection, simulation results for the RSC model applied to the NFA material are presented. The exponential top height distribution function (4.25) parameterized with the values given at the beginning of this chapter is plotted in figure 4.4. It specifies the number of tops with a specific height h, normalized by the crack area πR^2.

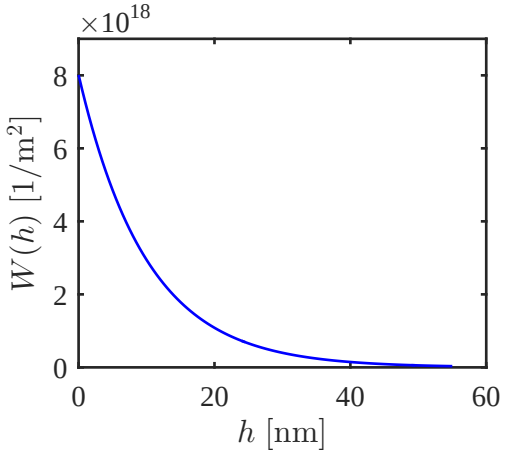

Figure 4.4: Exponential height distribution function.

The values of W for $h \geq 50\,\text{nm}$ are relatively small, which means that most of the

asperities are lower than 50 nm. This, in turn, implies that for a distance $d_0 \geq 50\,\text{nm}$ between the crack faces, the effect of the asperity contact must be relatively small.

Figure 4.5a shows the stress σ_0 to press the crack faces together as a dashed line, and the opposing stress σ_1 from compression of the asperities as a solid line. For the assumed initial crack opening d_0 = 30 nm, these stresses are equal per definition of the static equilibrium (4.28). The difference $\tilde{\sigma} = \sigma_0(d_0 + \tilde{d}) - \sigma_1(d_0 + \tilde{d})$ results from an incident wave.

Figure 4.5b depicts the function $\tilde{\sigma}$. The exact function is plotted as a solid line, the Taylor series approximation (4.31) dotted. A tensile stress $\tilde{\sigma} > 0$ corresponds to $\tilde{d} > 0$ and vice versa. For small crack distance variations $\tilde{d} = \pm\, 20\,\text{nm}$ the approximation matches the exact function well.

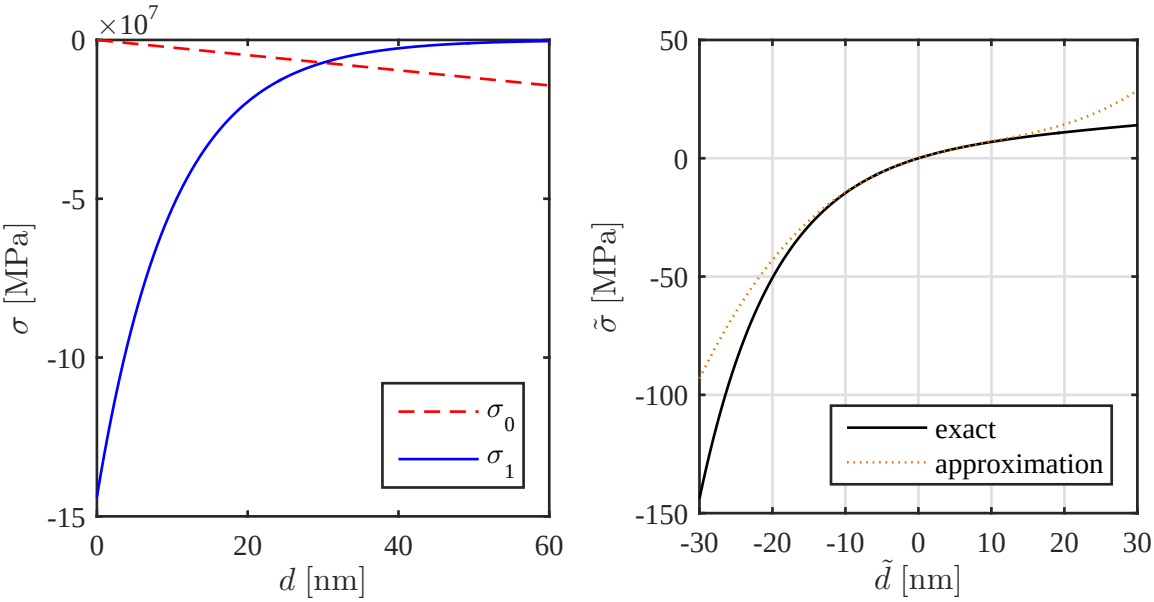

(a) Stresses on crack faces

(b) Dynamic stress due to wave with approximation

Figure 4.5: Stress-displacement relationships from RSC crack model.

The displacement $\tilde{d}$ = -30 nm corresponds to $d = d_0 + \tilde{d} = 0$, i.e. the complete closure of the crack. For this value, the Taylor series approximation deviates 35% from the exact $\tilde{\sigma}$. From the height distribution function, it was concluded that d = 50 nm describes an almost open crack. According to figure 4.5b, for this displacement the approximation leads to

30% bigger values for $\tilde{\sigma}$. This analysis shows that within the range of the admissible crack face motion the approximation made in determining $\tilde{\sigma}$ still leads to acceptable results. A more restrictive limitation, however, is the prerequisite $\tilde{d}/h_s \ll 2(1 + h_s/d_0)$ introduced by Nazarov and Sutin when they invert the relationship between $\tilde{\sigma}$ and $\tilde{d}$. It implies that a crack face distance variation of 20 nm may already lie outside of the range of validity of the model.

In order to interpret the stress σ_0 pressing the crack faces together, which is an auxiliary variable in the model, its influence on the acoustic nonlinearity parameter is shown in figure 4.6. If only a small stress is pressing the crack faces together, the acoustic nonlinearity is very high, because the cracks are wide open and strongly distort a propagating wave. Almost closed cracks under high values of σ_0 lead to a smaller acoustic nonlinearity parameter.

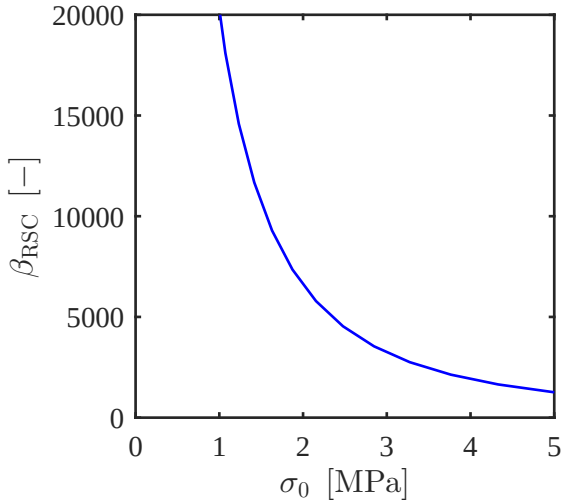

Figure 4.6: Acoustic nonlinearity β_{RSC} in RSC model as a function of internal stress σ_0 to press crack faces togehter.

Based on that microcrack model, the next step is to simulate the elastic behavior of the overall cracked solid. Figure 4.7 shows as a solid line the stress-strain relationship (4.21) up to the term ε^3. It becomes clear that the model can only be valid in a small range around $\varepsilon = 0$. Outside that range, $|\sigma|$ decreases for increasing $|\varepsilon|$ or even has a sign opposite of what is physically admissible. The maximum range of applicability is approximately

$-2 \cdot 10^{-4} \leq \varepsilon \leq 3 \cdot 10^{-4}$.

In the same figure, the stress-strain relationship only up to ε^2 is depicted as a dashed line. In the range around the origin in which the third-order polynomial is valid, it does not deviate much from the quadratic stress-strain curve. Although G_3 is multiple orders of magnitude larger than G_2, multiplying it with the third power of a small strain makes the resulting term relatively small. This implies that for the sufficiently small strains for which the RSC model leads to realistic results, there is only a small error if the cubic strain term is neglected. Moreover, since the focus of this research lies on the acoustic nonlinearity parameter $\beta_{\mathrm{RSC}} = G_2$, the term $(G_3/6)\varepsilon^3$ will be dropped in most of the following computations. As a reference, the figure shows the linear stress-strain relationship of the uncracked medium as a dot dashed line. The linear stress-strain relationship for tension from the bilinear stiffness model, which was introduced in figure 4.2, is depicted by the dotted line. The stiffness for compression in that model is equal to the stiffness of the uncracked solid.

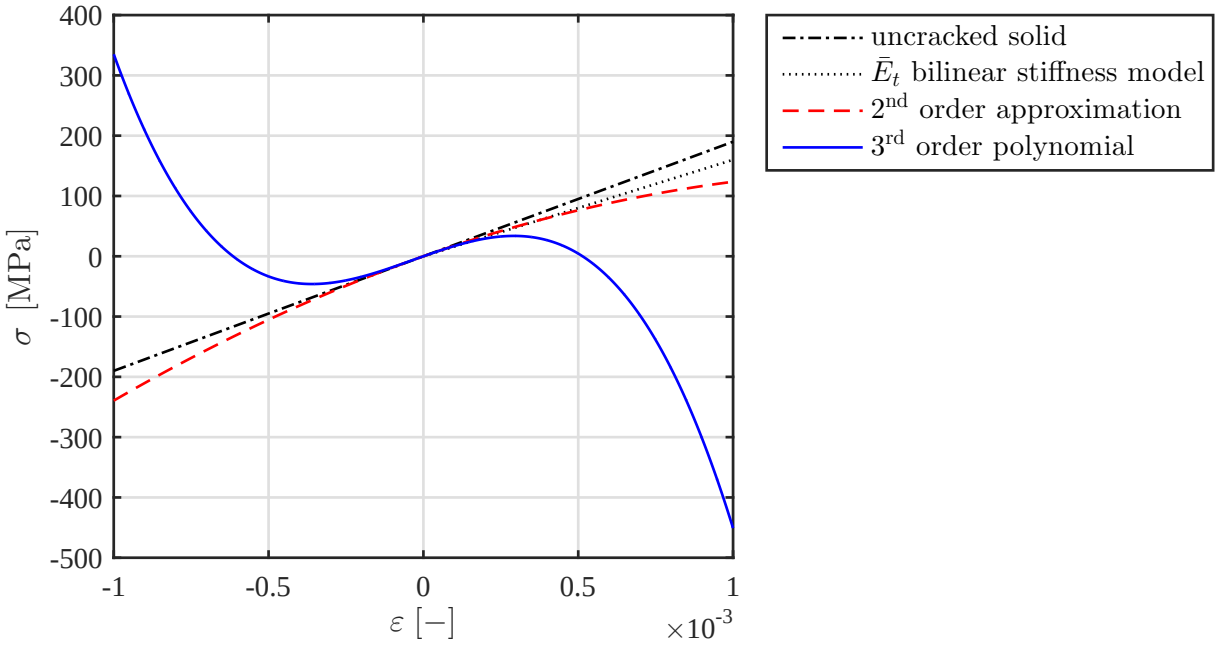

Figure 4.7: Effective stress-strain relationship of cracked solid from RSC model.

For the RSC microcrack model, various parameters had to be assumed, as explained in the introduction of this section. In the following paragraph, the influence of these parameters on the overall stress-strain relationship is examined. For every parameter variation, a figure of the following type will be given: The linear stress-strain relationship of the uncracked medium is plotted with a dashed line as a reference. The linear stress-strain relationship for tension from the bilinear stiffness model is shown as a green solid line.

1. **Varying Young's modulus E** has the effect depicted in figure 4.8a. For larger E, the slope of the stress-strain relationship from RSC increases. The term in ε^2 in (4.21) is proportional to E. Additionally, E enters nonlinearly in G_1. With increasing E, naturally also the slopes in the bilinear stiffness model increase.

2. **Varying Poisson's ratio ν**, which enters in G_1 and G_2, as well as in $\bar{E}_t$ has only a very small influence on the stress-strain relationship, see figure 4.8b.

3. **Varying the height of the roughness h_s** influences especially the stresses for negative strains, which corresponds to compression. For smaller top heights, more asperities lie within a certain height range, so that the absolute value of the stress to compress these is bigger, see figure 4.9a.

4. **Varying the initial crack opening d_0** has only a small influence on the stress-strain curve, where a smaller opening produces more nonlinearity, see figure 4.9b.

5. **Varying the number of cracks N_0**, as shown in figure 4.10a changes both models significantly.

6. **Varying the crack radius R** in figure 4.10b leads to a stronger nonlinear behavior for larger cracks.

As it becomes clear in equation (4.23), also the acoustic nonlinearity β_{RSC} depends on all of these parameters. Of particular interest is the dependency of the acoustic nonlinearity on the crack density, which is shown in figure 4.11a. Since the crack density $c = N_0 R^3$ used in the bilinear stiffness model incorporates the effect of the number of cracks and their size, a similar simulation is performed for the RSC model. In subfigure (a), the number of

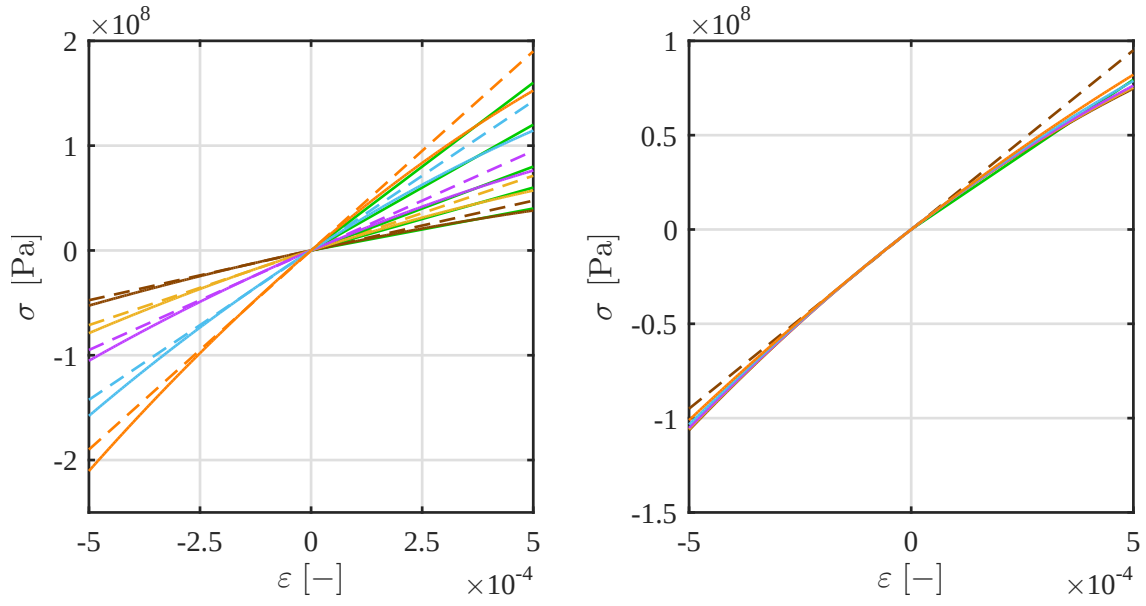

(a) Variable E (b) Variable ν

Figure 4.8: Stress-strain relationship in RSC model for variable material parameters. Nominal value (cf. table 4.1) times {0.5 (brown), 0.75 (yellow), 1 (purple), 1.5 (blue), 2 (orange)}

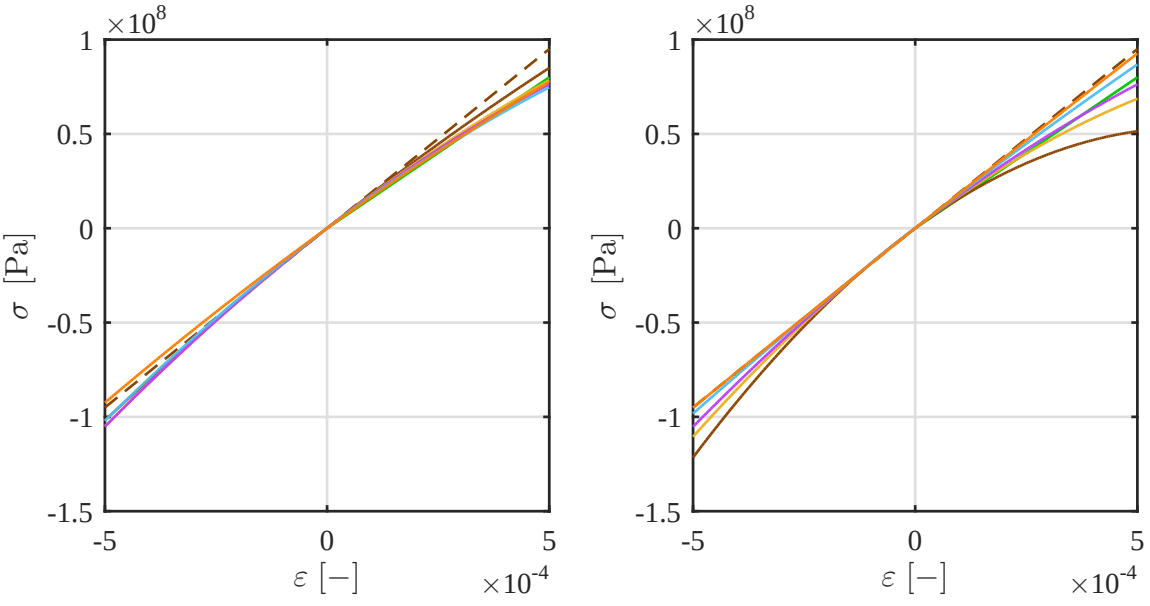

(a) Variable h_s (b) Variable d_0

Figure 4.9: Stress-strain relationship in RSC model for variable crack surface parameters. Nominal value (cf. table 4.1) times {0.3 (brown), 0.7 (yellow), 1 (purple), 2 (blue), 5 (orange)}

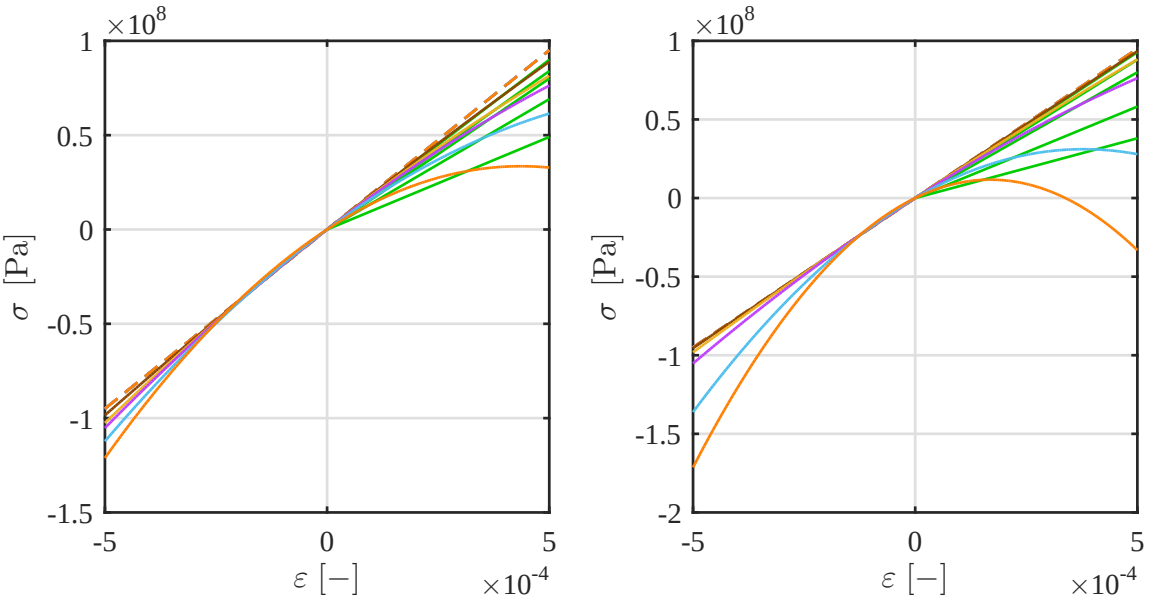

(a) Variable N_0. Nominal value (cf. table 4.1) times {0.3 (brown), 0.7 (yellow), 1 (purple), 2 (blue), 5 (orange)}

(b) Variable R. Nominal value (cf. table 4.1) times {0.5 (brown), 0.75 (yellow), 1 (purple), 1.5 (blue), 2 (orange)}

Figure 4.10: Stress-strain relationship in RSC model for variable material parameters that define the crack density $c = N_0 R^3$.

cracks per unit volume is varied, while their radius is kept constant at its nominal value 0.5 mm. As an example, the number $N_0 = 2 \cdot 10^9$ corresponds to $c = 0.25$. The acoustic nonlinearity increases with crack density, which matches physical intuition. For low crack densities the β_{RSC} values are approximately ten times as high as reported in the literature for polycrystals [9]. The function $\beta_{\mathrm{RSC}}(N_0)$ shows a similar trend as $\beta_B(c)$ in the bilinear stiffness model. However, the values of the acoustic nonlinearities β_B in the bilinear stiffness model (see figure 4.3) and β_{RSC} in the RSC model cannot be compared. The reason is that the underlying definitions of the acoustic nonlinearity parameter β are different in both models. The definitions were given in equation (2.15) for the RSC model and in equation (3.16) for the bilinear stiffness model, and the difference between them will be explained in more detail in the next section.

Subfigure (b) shows the influence of the crack size, while the number is kept constant at the nominal $3 \cdot 10^8$ cracks per m^3. Note that the crack radius enters the definition of the

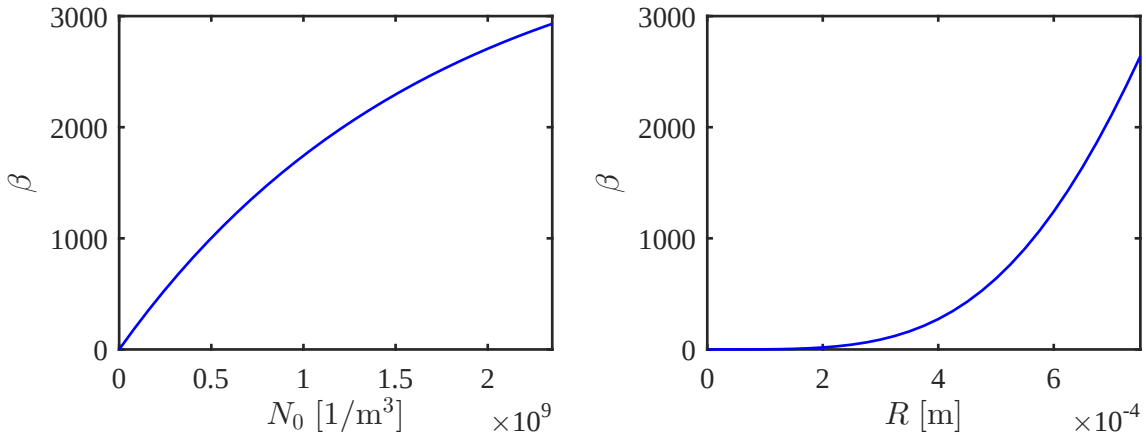

(a) Variable N_0.

(b) Variable R.

Figure 4.11: Dependency of acoustic nonlinearity β_{RSC} in RSC model on parameters that define the crack density $c = N_0 R^3$.

crack density as R^3. The acoustic nonlinearity increases significantly for cracks with radii larger than 0.5 mm. Large cracks, which are also too big to be defined as microcracks, are most likely at the boundary of the range of validity of the model.

4.3 Acoustic Nonlinearity Generation from Nonlinear Elastic Properties

The goal of this research is to model the relationship between the first and second harmonic amplitudes in a microcracked solid by combining the bilinear stiffness and RSC models. Technically, the papers on both of these models conclude with stating the acoustic nonlinearity parameter that specifies the required relationship [23], [35]. Thus, it might be intuitive to just add the nonlinearity from both effects. The significant difference, however, is that in both models the acoustic nonlinearity parameter is defined differently. The RSC model refers to the standard definition (2.15), in which A_2 is proportional to A_1^2. The bilinear stiffness model leads to another definition (3.16) with A_2 being proportional to A_1. Since the framework is so different, finding the relationship between A_1 and A_2 in a combined model becomes nontrivial and cannot be based on only using the final β results from both models. Therefore, the modeling of the mechanical properties of the cracked solid, which is the foundation for the acoustical model in the next step, plays a key role in this

research. This step becomes necessary because the overall stress-strain relationship can then be plugged into the wave equation in the next chapter, and the function $A_2(A_1)$ can be derived newly, without having to apply different definitions of β.

4.4 Overall Elastic Properties

4.4.1 Overall Nonlinear Stress-Strain Relationship

As described earlier, in this section, the three separate stress-strain relationships for the cases of tension, compression and asperity contact are combined into one overall stress-strain relationship of the cracked solid. It is obvious that this relationship must have three ranges, which is conceptually depicted in figure 4.12. For small strains there is asperity contact between the crack faces. For larger tensile strains, the cracks open up so that the effective tensile modulus $\bar{E}_t$ from the bilinear stiffness model holds. For compressive strains with large absolute values, the cracks are closed, so that the effective Young's modulus for compression $\bar{E}_c$ is equal to E of the uncracked solid.

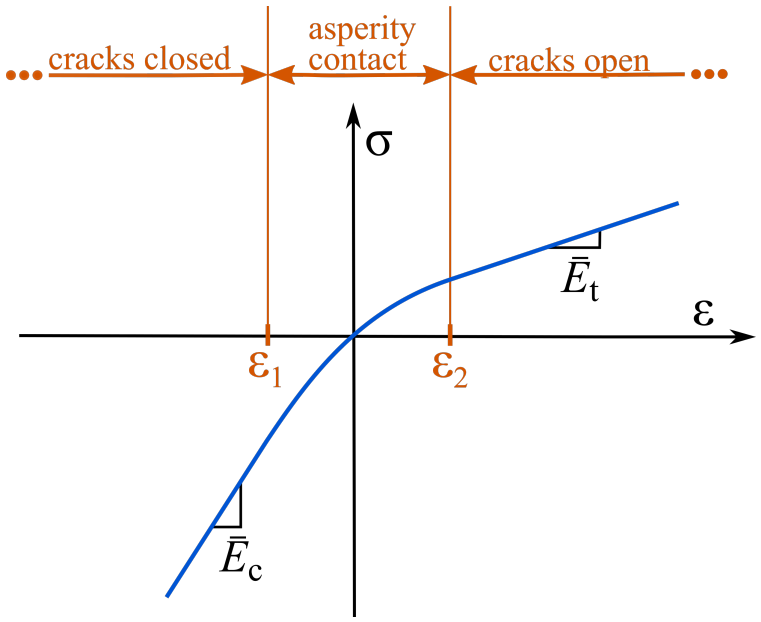

Figure 4.12: Overall nonlinear effective stress-strain relationship schematically.

Notably, the theoretical extension of the linear functions for completely open and closed cracks does not go through the origin. This results from the nonlinearity in the middle part of the stress-strain curve. It accounts for the stresses that are required to open up (respectively close) the cracks, so that this nonlinearity from asperity contact can clearly introduce some shift.

A crucial aspect in finding a model that combines the multiple effects is defining the transitions. More specifically, the strains ε_1, ε_2 and corresponding stresses at which the cracks open up, respectively, close completely have to be specified. Conceptually, there are two ways to define such transitions.

First, purely focusing on the microcrack model with RSC leads to geometrical argumentation. The cracks close completely if the distance variation $\tilde{d}$ compensates for the initial opening d_0, so that the resulting distance between the crack faces becomes zero. On the other hand, the cracks are open when d exceeds the height of the highest asperity. The stress-displacement curve in figure 4.5b for the crack being subjected to an incident wave specifies then the stresses at which the transitions take place. Subsequently, the corresponding strains result from the overall stress-strain curve in figure 4.7. This approach has two major disadvantages: Firstly, it is based on a microscopic, statistical model of the crack faces. Based on these statistics, defining a maximum height is not possible for the exponential distribution function, and also not for other typical distributions, such as Gaussian. Even if a height distribution with a finite maximum height, such as triangular were chosen, it would be challenging to argue based on statistical assumptions. Secondly, the RSC model assumes small $\tilde{d}$, so that crack face displacements as large as the ones necessary to open or close the crack entirely, may not be within the scope of the model.

The second approach to define a combined stress-strain relationship is based on the fact that the transition to completely open or closed cracks is a continuous process. Therefore, both the stress and the slope of the stress-strain curve must be continuous during the transition between the different crack states. Mathematically, in this research the transition is

defined where the stress-strain relationship from the RSC model has the same slope as the bilinear stiffness model. Since the stress-strain relationship in the RSC model is assumed to be quadratic, the second-order polynomial is fully defined by the two slopes at boundaries of the respective interval. It was shown in figure 4.12, that in order to obtain not only the same slope, but also the same stress from the bilinear stiffness model, the latter has to be shifted. The shifts in this approach for $\sigma_2 = \bar{E}_t\varepsilon_2 + c_2,\ \sigma_1 = \bar{E}_c\varepsilon_1 + c_1$ are determined as

$$\begin{aligned} &\sigma(\varepsilon_2) = EG_1\varepsilon_2 - \tfrac{1}{2}EG_1G_2\varepsilon_2^2 = \bar{E}_t\varepsilon_2 + c_2 \\ &\Leftrightarrow c_2 = (EG_1 - \bar{E}_t)\varepsilon_2 - \tfrac{1}{2}EG_1G_2\varepsilon_2^2 \end{aligned} \tag{4.34}$$

and equivalently

$$c_1 = (EG_1 - \bar{E}_c)\varepsilon_1 - \tfrac{1}{2}EG_1G_2\varepsilon_1^2. \tag{4.35}$$

Clearly, both shifts c_1 and c_2 have two reasons: First, they depend on the difference $(EG_1 - \bar{E}_i)$ in the linear term of the overall effective stress-strain relationship. Second, they contain a term depending on the quadratic nonlinearity $\frac{1}{2}EG_1G_2\varepsilon_i^2$ in the RSC model.

This approach to define the transition has the advantage that it is based on macroscopic, deterministic properties of the overall solid. Thus, it is preferred over the first one. Nevertheless, it must be underlined that in the literature on the RSC model, its range of applicability is clearly limited to small stresses. This is an important limitation of Nazarov and Sutin's model and beyond the boundaries, first, assumptions like linear elastic deformation may not hold anymore. Nevertheless, Greenwood and Williamson [11] found that elastic RSC is common in physical engineering practice applications. More recently, Kim and Lee [19] found that the unloading process is close to being elastic. Second, the stress-strain relationship results from approximately inverting the microcrack model, which is only valid for a sufficiently small range of crack face motion. Although using the results up to the limits of RSC can only be an approximation, it is an important step towards an analytical, more comprehensive model that accounts for multiple mechanisms in microcracks subjected to

an acoustic wave.

Next, the overall elastic properties of the cracked solid, which were qualitatively explained in the previous section and in figure 4.12, are formulated in terms of equations.

Since the stress-strain relationship consists of three distinct regions, it is defined piecewise in terms of Heaviside functions:

$$\begin{aligned}\sigma(\varepsilon) =& \Big(\bar{E}_c H[-(\varepsilon-\varepsilon_1)] + EG_1\big(H[\varepsilon-\varepsilon_1] - H[\varepsilon-\varepsilon_2]\big) + \bar{E}_t H[\varepsilon-\varepsilon_2]\Big)\varepsilon \\ & - \tfrac{1}{2}EG_1G_2\varepsilon^2\big(H[\varepsilon-\varepsilon_1] - H[\varepsilon-\varepsilon_2]\big) \\ & + H[-(\varepsilon-\varepsilon_1)]\big((EG_1-\bar{E}_c)\varepsilon_1 - \tfrac{1}{2}EG_1G_2\varepsilon_1^2\big) \\ & + H[\varepsilon-\varepsilon_2]\big((EG_1-\bar{E}_t)\varepsilon_2 - \tfrac{1}{2}EG_1G_2\varepsilon_2^2\big)\end{aligned} \tag{4.36}$$

The first line results from the different slopes in the linear part, the second line is the nonlinear term in ε^2 from the RSC model, and the last two lines quantify the shifts, since the bilinear relationship does not go through the origin of the stress-strain curve anymore.

4.4.2 Simulation

In a first step, the transitions between the different effects are calculated numerically, as described earlier in this section. In order to match the slopes, figure 4.13 depicts the derivative of the stress-strain relationship from the RSC model as a solid line. The dotted line shows the tensile and the dashed line the compressive effective modulus calculated in the bilinear stiffness model. The intersections of the function from the RSC model with the constant functions from the bilinear stiffness model define the transitions. Their numerical values are $\varepsilon_1 = -7.345 \cdot 10^{-5},\ \varepsilon_2 = 1.856 \cdot 10^{-4}$.

The same concept is applied in figure 4.14a for different parameters. Again, the dashed lines are the moduli from the bilinear stiffness model and the solid lines the slope of the stress-strain curve from RSC. In subfigure (a), Young's modulus is varied, and in subfigure

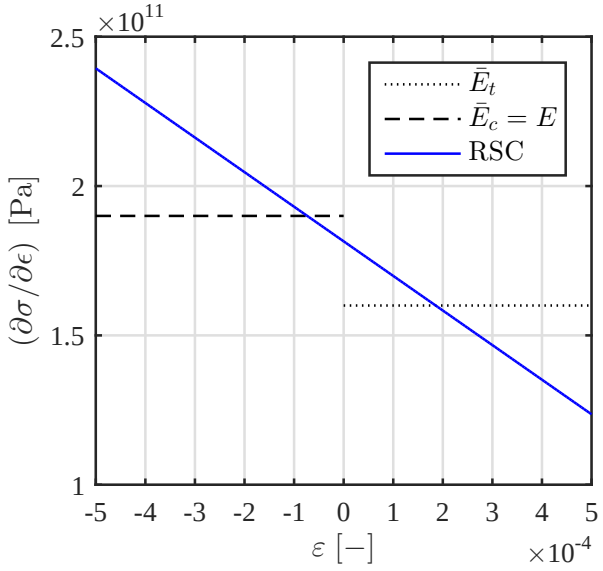

Figure 4.13: Derivatives of stress-strain relationships from both models.

(b) the crack density. Since the compressive modulus is independent of the crack density, it is equal in all cases in subfigure (b) and plotted as a black dashed line. The functions in purple are the nominal parameter values like in figure 4.13 as a reference. Both plots show that also for different Young's moduli and crack densities a smooth transition between both models exists.

Based on the transition strains ε_1 and ε_2, the combined stress-strain relationship (4.36) is computed and plotted in figure 4.15. The transitions, which are circled, are per definition continuous and continuously differentiable. The middle interval, in which the RSC model holds, shows only a slight nonlinearity, since the term in ε^2 is small for small strains. However, it was seen earlier in this section that the acoustic nonlinearity from the RSC model is large, so that it has a significant impact on the acoustic model which will be formulated in the next chapter.

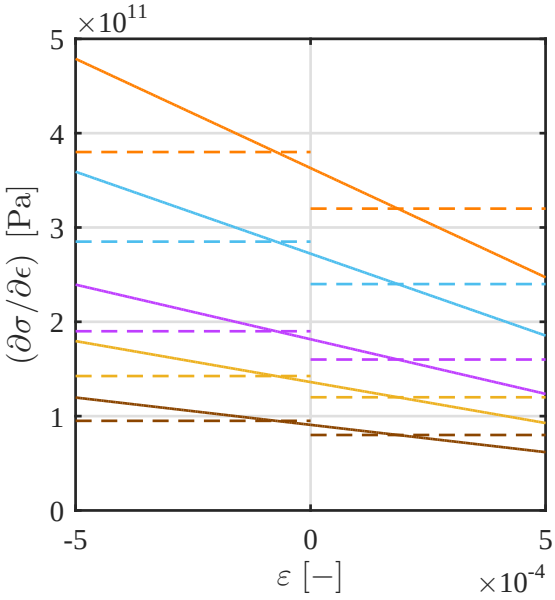

(a) Variable $E = \{95$ (brown), 142.5 (yellow) 190 (purple), 285 (blue), 380 (orange)$\}$ GPa.

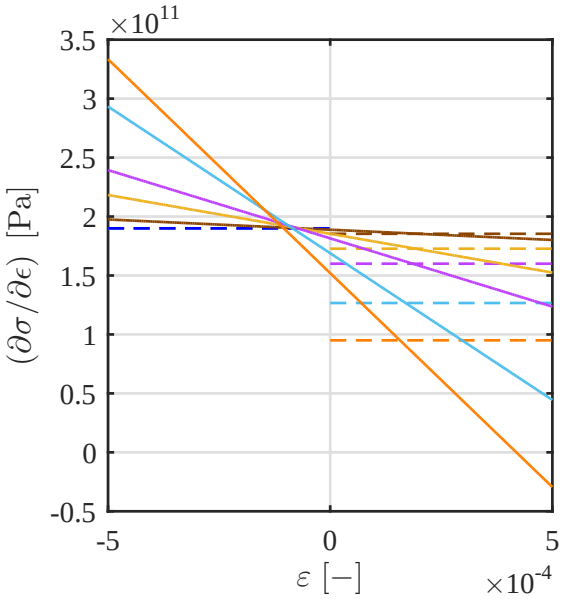

(b) Variable $c = \{0.005$ (brown), 0.02 (yellow) 0.0375 (purple), 0.1 (blue), 0.2 (orange)$\}$.

Figure 4.14: Derivatives of stress-strain relationships: dependency on parameters.

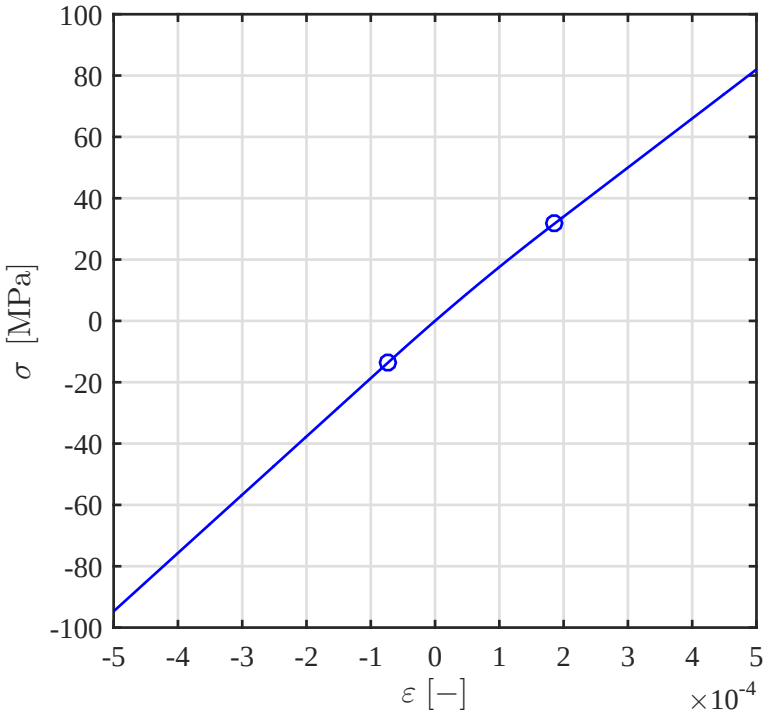

Figure 4.15: Overall nonlinear effective stress-strain relationship numerically.

4.4.3 Micromechanical Averaging for the Asperity Contact Case

In their paper, Nazarov and Sutin [23] set up a microcrack model first and then formulate a calculation procedure to determine the additional strain resulting from the crack. An alternative approach is to use only their microcrack model from the first step, and then plug it into a different framework, namely an averaging scheme commonly applied in the field of micromechanics. The elastic properties E_1, ν_1 of a crack, which are required in such a micromechanical averaging scheme, can be specified in two different ways. An approximate way is to define the crack as a void with zero stiffness and zero lateral contraction. The approach that will be taken in this thesis is to model the crack as a Hertzian contact, whose stiffness is obtained from the RSC model. In this section, Nazarov and Sutin's crack model is considered as a stand-alone method that is combined with a micromechanical averaging schemes to obtain the effective moduli of a cracked solid later.

As before, consider a crack in the dynamic equilibrium $\tilde{\sigma} = \sigma_0(d_0 + \tilde{d})\sigma_1(d_0 + \tilde{d})$. By linearizing $\tilde{\sigma}$ around d_0, the linear stiffness parameter of the interface is introduced as

$$k_\sigma = \left.\frac{\mathrm{d}\tilde{\sigma}}{\mathrm{d}d}\right|_{d_0} = \frac{3\pi E}{(16R(1-\nu^2))} + nE_1/h_s \exp(-d_0/h_s); \tag{4.37}$$

to be applied in $\Delta\tilde{\sigma}(\Delta\tilde{d}) = k_\sigma \Delta\tilde{d}$. This newly defined parameter can be mapped to the force domain to model the spring-like elastic behavior of the crack as

$$k_F = k_\sigma A_{\text{crack}} \tag{4.38}$$

$$\Delta F_{\text{lin}} = k_F \Delta\tilde{d}. \tag{4.39}$$

By defining the strain in the crack as $\varepsilon = \Delta\tilde{d}/d_0$ and plugging into $\Delta F_{\text{lin}}/A = E_{1,\text{lin}}\varepsilon$, the Young's modulus of the crack becomes

$$E_{1,\text{lin}} = \frac{k_F}{A_{\text{crack}} d_0}. \tag{4.40}$$

With the parameter values given at the beginning of this section, it is $E_{1,\text{lin}} = 2.8651 \cdot 10^7$, which is multiple orders of magnitude smaller than of the uncracked solid. Plugging this value for E_1 into the Mori-Tanaka averaging scheme explained in chapter 3.3, yields the average modulus of the cracked material $\bar{E}_a = 178.46\,\text{GPa}$. As expected, the cracks reduce the overall stiffness of the material.

Since the stiffness of the crack is found to be significantly smaller than the stiffness E, a comparison to a void with zero stiffness is made next. For $E_1 = 0$ and the same crack density $c_1 = 0.0375$, the Mori-Tanaka method leads to the same effective modulus $\bar{E}_a = 178.46\,\text{GPa}$ of the cracked material. This means that the effect of RSC becomes negligible in a micromechanical averaging scheme.

There are multiple reasons for this observation:

First, the definition of the local strain on the crack is critical. In the previous paragraph it was defined as $\varepsilon = \Delta\tilde{d}/d_0$, which leads to very large strains if the distance between the crack faces deviates significantly from the initial opening d_0. However, there is no other straight-forward calculation of the strain in terms of physical quantities from the crack model, so that more complex considerations of the displacement and strain field would be necessary.

Second, linearizing the dynamic stress $\tilde{\sigma}$ is a simplification that is only valid locally. Figure 4.16a shows the acoustic stress $\tilde{\sigma}$ as a function of the displacement $\tilde{d}$ due to the wave, and its linearization around the origin. It becomes clear that the highly nonlinear stress-displacement curve deviates strongly from its linearization, even for displacements as small as $10\,\text{nm}$.

Without linearization, another approach is taken: based on the nonlinear function $\tilde{\sigma}(\tilde{d})$, the local Young's modulus is defined as

$$E_{\text{local}} = \tilde{\sigma}\frac{d_0}{\tilde{d}}, \qquad \tilde{d} \neq 0 \tag{4.41}$$

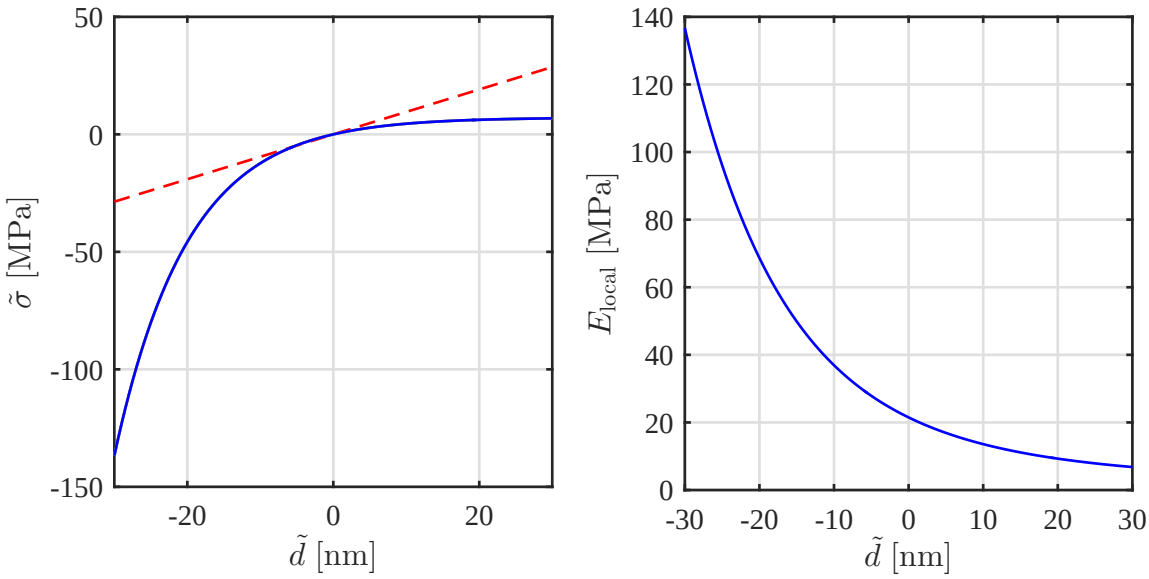

(a) Linearization of $\tilde{\sigma}$.

(b) Definition of a local Young's modulus from $\tilde{\sigma}$.

Figure 4.16: Numerical calculation of the crack stiffness.

This approach accounts for the nonlinear stress-displacement relationship, and leads to the nonlinear function $E_{\mathrm{local}}(\tilde{d})$, which is depicted in figure 4.16b. It shows that the stiffness of the interface increases the more the asperities become deformed.

Nevertheless, as E_{local} is still decades smaller than E, simulations show that it still becomes negligible in the averaging scheme. The reason, again, is the simplified definition of ε, as explained above, due to which large strains and, consequently, small stiffnesses for a given crack stress are calculated. Because of this disadvantage, Nazarov and Sutin's approach [23] to integrate the RSC crack model is more appropriate than applying a micromechanical averaging scheme using a simplified spring-like consideration.

4.4.4 Overall Trilinear Stress-Strain Relationship

In subsection 4.4.1, a combined stress-strain relationship that includes all three crack states – closed, asperity contact and open – was introduced. Therein, the stress-strain curve for asperity contact is nonlinear. In contrast, in the previous subsection a linear stress-strain curve was calculated for the asperity contact state, using micromechanical averaging.

To facilitate the derivation of the crack-wave interactions in the next chapter, it is useful to split the overall problem into a linear and a nonlinear part. For completely open and completely closed cracks, the model is naturally linear, resulting from the bilinear stiffness approach. For asperity contact, the RSC stress-strain relationship $\sigma(\varepsilon) = EG_1(\varepsilon + G_2\varepsilon^2/2)$ can be split into the linear term $EG_1 = \bar{E}_a$ and the nonlinear term $EG_1G_2/2$. Alternatively, for asperity contact a linear stress-strain curve with slope $\bar{E}_{a,\text{lin}}$ from an averaging scheme, as described in the previous subsection, can be used. Both apporaches lead to a trilinear stress-strain relationship, which is, despite the underlying approximations, a more comprehensive model than only bilinear stiffness or purely RSC. Figure 4.17 shows such a trilinear stress-strain relationship.

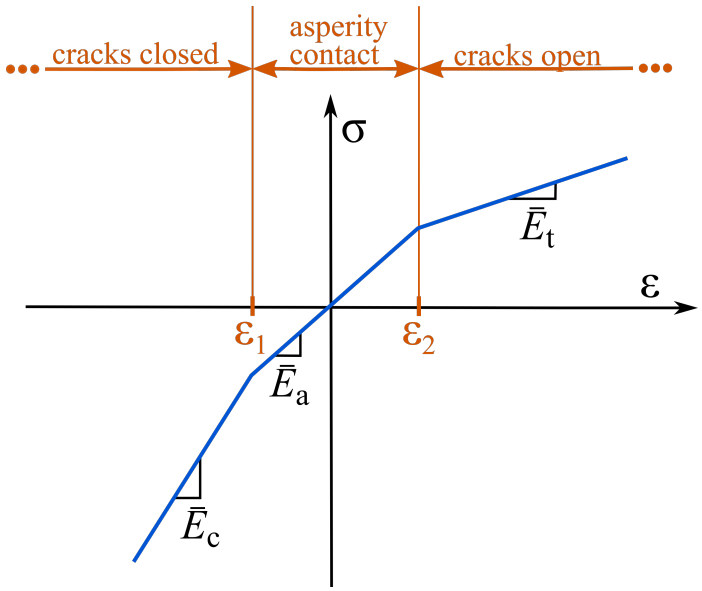

Figure 4.17: Trilinear effective stress-strain relationship.

It is mathematically specified by

$$\begin{aligned}\sigma(\varepsilon) =& \Big(\bar{E}_c H[-(\varepsilon-\varepsilon_1]) + \bar{E}_a\big(H[\varepsilon-\varepsilon_1] - H[\varepsilon-\varepsilon_2]\big) + \bar{E}_t H[\varepsilon-\varepsilon_2]\Big)\varepsilon \\ &+ H[-(\varepsilon-\varepsilon_1)](EG_1 - \bar{E}_c)\varepsilon_1 \\ &+ H[\varepsilon-\varepsilon_2](EG_1 - \bar{E}_t)\varepsilon_2,\end{aligned} \tag{4.42}$$

where the linear term EG_1 from asperity contact is abbreviated as $\bar{E}_a$. Young's modulus

for compression $\bar{E}_c$, which was found to be equal to the modulus of the uncracked solid in section 4.1, is chosen as a reference. Then the relative quantities

$$\gamma_c = \frac{\bar{E}_c - \bar{E}_a}{\bar{E}_c}, \qquad \gamma_c = \frac{\bar{E}_t - \bar{E}_a}{\bar{E}_c} \tag{4.43}$$

are introduced, so that (4.42) is rewritten as

$$\begin{aligned} \sigma(\varepsilon) =& \bar{E}_c\big(1 - \gamma_c H[\varepsilon - \varepsilon_1] + \gamma_t H[\varepsilon - \varepsilon_2]\big)\varepsilon \\ &+ \bar{E}_c\big(- \gamma_c \varepsilon_1 + \gamma_c H[\varepsilon - \varepsilon_1]\varepsilon_1 - \gamma_t H[\varepsilon - \varepsilon_2]\varepsilon_2\big), \end{aligned} \tag{4.44}$$

where $H[-x] = 1 - H[x]$ was applied.

This stress-strain relationship will be the basis of the following chapter.

CHAPTER 5
NONLINEAR INTERACTIONS BETWEEN ULTRASONIC WAVES AND MICROCRACKS

In the previous chapter, the combined stress-strain relationship, which includes effects from both the bilinear stiffness model and the RSC model, has been derived. Based on these overall nonlinear elastic properties of the cracked solid, the interactions with ultrasonic waves will be examined next.

The nonlinear stress-strain relationship can be split up into a trilinear part being present for all strains, and a nonlinear part resulting from asperity contact and being present in the interval $\varepsilon_1 \leq \varepsilon \leq \varepsilon_2$. Both contributions are treated separately, because the overall nonlinear stress-strain relationship is a superposition of them. These two contributions correspond to two different mechanisms that generate acoustic nonlinearity.

The first mechanism is the elastic deformation of the asperities in Nazarov and Sutin's RSC model. The nonlinear term $EG_1\beta_{\mathrm{RSC}}\varepsilon^2/2$ from that model causes a second harmonic wave of amplitude $A_{2,RSC} = (\beta_{\mathrm{RSC}}A_1^2 x\omega^2)/(8c_L^2)$. This can be easily seen by plugging the nonlinear stress-strain relationship $\sigma_{\mathrm{RSC}}(\varepsilon) = EG_1(\varepsilon - \beta_{\mathrm{RSC}}\varepsilon^2/2)$ into the governing equation (2.2). Therefore, the influence of this term, being proportional to ε^2, on the wave equation is mathematically already understood well.

The second mechanism that generates acoustic nonlinearity is the change in the elastic moduli for the three crack states open, asperity contact and closed. This corresponds to the trilinear part of the stress-strain curve with slopes $\bar{E}_t, \bar{E}_a, \bar{E}_c$. Such a trilinear stress-strain relationship has not been formulated in the literature yet. Thus, also its effect on acoustic waves has not been examined yet.

In their paper, Zhao et al. [35] use the bilinear stiffness model, solve the resulting nonlinear wave equation and take the Fourier transform to calculate the amplitude of the

second harmonic wave. The present thesis extends their piecewise formulation of the stress-strain relationship from the bilinear to the trilinear case. As it was stated in the previous chapter, also the term depending on ε^2 is superimposed, but treated separately.

The derivation in this chapter uses the idea of Zhao et al. [35] to consider the additional terms resulting from the change in elastic moduli as a perturbation to the linear wave equation. Nevertheless, the derivation will be carried out differently from theirs to account for the more complex structure of equations in the trilinear case.

5.1 Derivation of the Overall Displacement Equation of Wave Motion

The derivative of the trilinear part of the overall stress-strain relationship (4.44), which has to be plugged into the wave equation (2.2), is the following:

$$\begin{aligned}\frac{\partial \sigma}{\partial x} =& \bar{E}_c \frac{\partial^2 u}{\partial x^2} \\ &- \bar{E}_c \Big(\gamma_c H[\frac{\partial u}{\partial x} - \varepsilon_1] - \gamma_t H[\frac{\partial u}{\partial x} - \varepsilon_2] + \big(\gamma_c \delta[\frac{\partial u}{\partial x} - \varepsilon_1] - \gamma_t \delta[\frac{\partial u}{\partial x} - \varepsilon_2] \big) \frac{\partial u}{\partial x} \Big) \frac{\partial^2 u}{\partial x^2} \\ &- \bar{E}_c \Big(\gamma_t \varepsilon_2 \delta[\frac{\partial u}{\partial x} - \varepsilon_2] - \gamma_c \varepsilon_1 \delta[\frac{\partial u}{\partial x} - \varepsilon_1] \Big) \frac{\partial^2 u}{\partial x^2}.\end{aligned} \tag{5.1}$$

The first term is the one from the linear wave equation, the second line stems from the discontinuous slopes, and the third line results from the shift of the bilinear stiffness. Therein, define the following functions

$$f_t(u) = \frac{\partial}{\partial x} \Big(H[\frac{\partial u}{\partial x} - \varepsilon_2] \frac{\partial u}{\partial x} \Big) = \delta[\frac{\partial u}{\partial x} - \varepsilon_2] \frac{\partial^2 u}{\partial x^2} \frac{\partial u}{\partial x} + H[\frac{\partial u}{\partial x} - \varepsilon_2] \frac{\partial^2 u}{\partial x^2} \tag{5.2a}$$

$$f_c(u) = \frac{\partial}{\partial x} \Big(H[\frac{\partial u}{\partial x} - \varepsilon_1] \frac{\partial u}{\partial x} \Big) = \delta[\frac{\partial u}{\partial x} - \varepsilon_1] \frac{\partial^2 u}{\partial x^2} \frac{\partial u}{\partial x} + H[\frac{\partial u}{\partial x} - \varepsilon_1] \frac{\partial^2 u}{\partial x^2} \tag{5.2b}$$

$$f_{t,\text{shift}}(u) = \frac{\partial}{\partial x} \Big(H[\frac{\partial u}{\partial x} - \varepsilon_2] \Big) = \delta[\frac{\partial u}{\partial x} - \varepsilon_2] \frac{\partial^2 u}{\partial x^2} \tag{5.2c}$$

$$f_{c,\text{shift}}(u) = \frac{\partial}{\partial x} \Big(H[\frac{\partial u}{\partial x} - \varepsilon_1] \Big) = \delta[\frac{\partial u}{\partial x} - \varepsilon_1] \frac{\partial^2 u}{\partial x^2}. \tag{5.2d}$$

For brevity, introduce $H_1 \equiv H[\varepsilon - \varepsilon_1],\ H_2 \equiv H[\varepsilon - \varepsilon_2],\ \delta_1 \equiv \delta[\varepsilon - \varepsilon_1],\ \delta_2 \equiv \delta[\varepsilon - \varepsilon_2]$. Plugging everything in the wave equation (2.2) yields

$$\rho\frac{\partial^2 u}{\partial t^2} = \bar{E}_c\frac{\partial^2 u}{\partial x^2} - \bar{E}_c\Big(\gamma_c H_1 - \gamma_t H_2 + \gamma_c\big(\frac{\partial u}{\partial x} - \varepsilon_1\big)\delta_1 - \gamma_c\big(\frac{\partial u}{\partial x} - \varepsilon_2\big)\delta_2\Big)\frac{\partial^2 u}{\partial x^2} \tag{5.3}$$

and, consequently,

$$\frac{\partial^2 u}{\partial t^2} - c_{L,c}^2\frac{\partial^2 u}{\partial x^2} = -c_{L,c}^2\big(\gamma_c(f_c - f_{c,\text{shift}}) - \gamma_t(f_t - f_{t,\text{shift}})\big). \tag{5.4}$$

where $c_{L,c}^2 = \sqrt{\bar{E}_c/\rho}$ is the longitudinal wave velocity using the effective compressive modulus $\bar{E}_c$.

5.2 Perturbation Method

The nonlinear wave equation (5.4) and its respective boundary conditions form a nonlinear boundary value problem (BVP).

This problem can be solved approximately using a perturbation method, as presented by Cantrell in [8]. To this end, the solution for the total displacement field u is split up into $u = u_1 + u_2$. In this expression, u_1 is the solution to the linear wave equation, to which a higher order perturbation u_2 is added. The perturbation method is only applicable if $|u_2| \ll |u_1|$. This is usually fulfilled in the case of the generation of second harmonic waves, where the amplitude of the second harmonic is much smaller than of the incident wave.

This solution approach is plugged into the nonlinear wave equation (5.4). On the right-hand side of the equation, the terms $\gamma_i H_i$ and $\gamma_i \delta_i$ are of order $\mathcal{O}(1)$, whereas $\frac{\partial u}{\partial x} = \varepsilon$ and $\frac{\partial^2 u}{\partial x^2}$ are much smaller than 1. As seen in the previous section, the relative change in the second-order elastic constants is small ($\gamma_t, \gamma_c \ll 1$), so that the terms $u_i,\ i = \mathrm{t}, \mathrm{c}, \mathrm{a}$ are of order $\mathcal{O}(\gamma_i u_1)$ [35]. Consequently, the terms in $|u_2 u_2|$, $|u_1 u_2|$ and their derivatives on the right-hand side are much smaller than $|u_1 u_1|$ and its derivatives, so that the former can be

neglected.

The idea in the perturbation method is then to decompose the remaining PDE. First, the linear homogeneous BVP

$$\frac{\partial^2 u_1}{\partial t^2} - c_{L,c}^2 \frac{\partial^2 u_1}{\partial x^2} = 0 \tag{5.5}$$

is separated from the rest. From this problem, the solution u_1 is calculated. Similar to [35], consider the wave propagation for $t \leq 0$ in the half space $x > 0$ induced by a prescribed excitation $u(0,t) = A_1 \sin(\omega t)$ at the boundary $x = 0$. A solution to the linear wave equation (5.5) is

$$u_1(x,t) = A_1 \sin(\omega t - kx). \tag{5.6}$$

Then, u_1 acts as a perturbation term on the right-hand side of the remaining inhomogeneous problem

$$\begin{aligned} &\frac{\partial^2 u_2}{\partial t^2} - c_{L,c}^2 \frac{\partial^2 u_2}{\partial x^2} \\ &= -c_{L,c}^2 \Big(\gamma_c H_1[u_1] - \gamma_t H_2[u_1] + \big(\gamma_c \delta_1[u_1] - \gamma_c \delta_2[u_1] \big) \frac{\partial u_1}{\partial x} \Big) \frac{\partial^2 u_1}{\partial x^2} \\ &= -c_{L,c}^2 (\gamma_c f_c - \gamma_t f_t - \gamma_c f_{c,\text{shift}} + \gamma_t f_{t,\text{shift}}), \end{aligned} \tag{5.7}$$

where f_i are defined in equations (5.2a) to (5.2d). In order to solve this equation for u_2, the right-hand side has to be analyzed in more detail.

Since the displacement solution $u_2(x,t)$ results from the nonlinearity in the stress-strain relationship, it is a linear combination of the nonlinearities produced by each term in equation 5.1. Therefore, let

$$u_2(t,x) = u_t(t,x) + u_c(t,x) + u_{t,\text{shift}}(t,x) + u_{c,\text{shift}}(t,x). \tag{5.8}$$

The BVPs for $u_i(x,t)$ resulting from the perturbation method are addressed independently in the following and added afterwards.

The solution will be developed in detail for the tension term f_t and then adapted to the

other segments of the stress-strain curve. In the case of tension, the perturbation method leads to the following BVP:

$$\frac{\partial^2 u}{\partial t^2} - c_{L,c}^2 \frac{\partial^2 u}{\partial x^2} = -c_{L,c}^2 \gamma_t f_t(u_1) \tag{5.9a}$$

$$u_t(0,t) = 0 \tag{5.9b}$$

$$u_t(x,t) = 0 \quad \text{for } t \leq 0. \tag{5.9c}$$

Since the goal is to calculate the amplitude of the first, second, etc. harmonic, a Fourier series expansion of the right-hand side, more specifically the function

$$\begin{aligned} f_t(u_1) = A_1^2 k^3 \delta\big[- A_1 k \cos(\omega t - kx) - \varepsilon_2\big] \sin(Y) \cos(Y) \\ - A_1 k^2 H\big[- A_1 k \cos(Y) - \varepsilon_2\big] \sin(Y) \end{aligned} \tag{5.10}$$

will be computed next. This function, as well as all other f_i, is 2π periodic in the argument $\omega t - kx$, which is substituted with Y in the following.

The next paragraph gives a brief overview of basic Fourier series theory. Every periodic function can be represented as the sum of sines and cosines. More specifically, any 2π-periodic function can be written as a series

$$f(Y) = \frac{a_0}{2} + \sum_{n=1}^{\infty} \big(a_n \cos(nY) + b_n \sin(nY)\big) \tag{5.11}$$

with Fourier coefficients

$$a_0 = \frac{1}{\pi} \int_{-\pi}^{\pi} f(Y)\, \mathrm{d}Y \tag{5.12a}$$

$$a_n = \frac{1}{\pi} \int_{-\pi}^{\pi} f(Y) \cos(nY)\, \mathrm{d}Y \tag{5.12b}$$

$$b_n = \frac{1}{\pi} \int_{-\pi}^{\pi} f(Y) \sin(nY)\, \mathrm{d}Y \tag{5.12c}$$

When computing the Fourier coefficients for the term f_t, multiple terms depend on the

transitions, such as $H[\frac{\partial u}{\partial x} - \varepsilon_2]$ and $\delta[\frac{\partial u}{\partial x} - \varepsilon_2]$. This implies evaluating the function $\frac{\partial u}{\partial x}$ at ε_2, so that $\varepsilon_2 = \frac{\partial u}{\partial x} = -kA_1 \cos(Y_2)$. The solution to this equation will be abbreviated as

$$Y_2 = \arccos\Big(\frac{-\varepsilon_2}{kA_1}\Big). \tag{5.13}$$

Using this result, the calculation of the Fourier coefficients yields: $a_n = 0 \quad \forall\, n$ because the function f_t is odd,

$$\begin{aligned} b_{n,t} = \frac{A_1 k^2}{\pi}\Big(&2A_1 k \sin(Y_2)\cos(Y_2)\sin(nY_2) \\ &+ \frac{2}{n^2-1}\big(\cos(Y_2)\sin(nY_2) - n\sin(Y_2)\cos(nY_2)\big)\Big) \end{aligned} \tag{5.14}$$

for $n \geq 2$,

and separately $b_{1,t} = \frac{A_1 k^2}{\pi}\big(2A_1 k \sin^2(Y_2)\cos(Y_2) + Y_2 - \pi - \sin(Y_2)\cos(Y_2)\big)$. It becomes clear that due to the argument Y_2 the Fourier coefficients do not only depend on the strain ε_2 at which the cracks open up, but also indirectly on the amplitude A_1 and the wave number.

With this Fourier series expansion, the PDE (5.9a) becomes

$$\frac{\partial^2 u}{\partial t^2} - c_{L,c}^2 \frac{\partial^2 u}{\partial x^2} = -c_{L,c}^2 \gamma_t \big(b_{1,t}\sin(Y) + b_{2,t}\sin(2Y) + b_{3,t}\sin(3Y) + \cdots\big). \tag{5.15}$$

Due to its decoupled structure, this equation can be solved separately for each harmonic.

The solution procedure is carried out exemplarily for the perturbation equation

$$\frac{\partial^2 u_t}{\partial t^2} - c_{L,c}^2 \frac{\partial^2 u_t}{\partial x^2} = -c_{L,c}^2 \gamma_t b_{2,t}\sin(2Y) \tag{5.16}$$

Following the computation of [8], a general solution of the form

$$u_{2,t}(x,t) = h_{2,t}(x)\sin\big(2(\omega t - kx)\big) + g_{2,t}(x)\cos\big(2(\omega t - kx)\big) \tag{5.17}$$

is assumed. To satisfy the boundary condition that the second harmonic vanishes at $x = 0$,

the functions $h_{2,t}(x)$ and $g_{2,t}(x)$ have to be zero at $x = 0$. Substituting the solution approach (5.17) into equation (5.16) yields

$$\begin{aligned}
&- 4\omega^2 f_{2,t}(x)\sin(2Y) - 4\omega^2 g_{2,t}(x)\cos(2Y) \\
&- c_{L,c}^2\Big(\frac{\mathrm{d}^2 h_{2,t}(x)}{\mathrm{d}x^2}\sin(2Y) - 4k\frac{\mathrm{d}h_{2,t}(x)}{\mathrm{d}x}\cos(2Y) - 4k^2 h_{2,t}(x)\sin(2Y) \\
&\qquad + \frac{\mathrm{d}^2 g_{2,t}(x)}{\mathrm{d}x^2}\cos(2Y) + 4k\frac{\mathrm{d}g_{2,t}(x)}{\mathrm{d}x}\sin(2Y) - 4k^2 g_{2,t}(x)\cos(2Y)\Big) \\
&= -\gamma_t c_{L,c}^2 b_{2,t}\sin(2Y).
\end{aligned} \tag{5.18}$$

In order to satisfy this equation, the following conditions for the coefficients of the sine respectively cosine terms must be fulfilled:

$$1. \qquad 4k\frac{\mathrm{d}h_{2,t}}{dx} - \frac{\mathrm{d}^2 g_{2,t}}{\mathrm{d}x^2} = 0 \tag{5.19}$$

$$2. \qquad -\frac{\mathrm{d}^2 h_{2,t}}{\mathrm{d}x^2} - 4k\frac{\mathrm{d}g_{2,t}}{\mathrm{d}x} = -\gamma_t b_{2,t} \tag{5.20}$$

A consistent solution to these two equations is calculated if it is assumed that $\frac{\mathrm{d}h_{2,t}}{\mathrm{d}x} = 0$ and $\frac{\mathrm{d}^2 g_{2,t}}{\mathrm{d}x^2} = 0$. This implies that, first, $h_{2,t}(x) = \text{const.} = h_0$. Since $h_{2,t}(x)$ has to vanish at the boundary, $h_0 = 0$. Second, it must hold that $\frac{\mathrm{d}g_{2,t}}{\mathrm{d}x} = \text{const.} = g_1$. Plugging into equation (5.19) leads to $4kg_1 = \gamma_t b_{2,t}$, from which it can be concluded by integration

$$g_{2,t}(x) = \frac{\gamma_t b_{2,t} x}{4k}. \tag{5.21}$$

Therefore, the solution for the second harmonic amplitude due to the change in Young's modulus in the tensile case is

$$u_{2,t}(x,t) = \frac{\gamma_t b_{2,t} x}{4k}\cos\big(2(\omega t - kx)\big). \tag{5.22}$$

The other harmonics are computed in a similar manner.

This yields $u_{1,t} = \frac{\gamma_t b_{1,t} x}{k} \cos(\omega t - kx)$, and generally

$$u_{n,t} = \frac{\gamma_t b_{n,t} x}{n^2 k} \cos\big(n(\omega t - kx)\big). \tag{5.23}$$

Beyond that, the segment of the stress-strain relationship for the tensile case contains a constant shift, whose Fourier series and influence on the second harmonic amplitude will be calculated next. The term $f_{t,\text{shift}} = \delta\big[-A_1 k \cos(Y) - \varepsilon_2\big](-A_1)k^2 \sin(Y)$ leads to the additional Fourier coefficients

$$b_{n,t,\text{shift}} = \frac{-2A_1 k^2}{\pi} \sin(Y_2) \sin(nY_2). \tag{5.24}$$

As $f_{t,\text{shift}}$ enters the perturbation equation (5.7) in the same way as f_t, it can be inserted directly into the result (5.23)

$$u_{n,t,\text{shift}}(x) = \frac{\gamma_t b_{n,t,\text{shift}} x}{n^2 k} \cos\big(n(\omega t - kx)\big). \tag{5.25}$$

In the derivative of the stress-strain relationship the term for completely closed cracks under compression is structurally similar to the tension term that was worked on in the previous paragraph. Consequently, the same procedure will be applied for compression. Define the term depending on the transition ε_1 as $Y_1 = \arccos(\frac{-\varepsilon_1}{kA_1})$. The excitation term f_c leads to the Fourier coefficients $a_n = 0 \quad \forall\, n$,

$$\begin{aligned} b_{n,c} = \frac{A_1 k^2}{\pi} \Big(& 2A_1 k \sin(Y_1) \cos(Y_1) \sin(nY_1) \\ & + \frac{2}{n^2 - 1} \big(\cos(Y_1) \sin(nY_1) - n \sin(Y_1) \cos(nY_1) \big) \Big) \end{aligned} \tag{5.26}$$

for $n \geq 2$ and $b_{1,c} = \frac{A_1 k^2}{\pi} \big(2A_1 k \sin^2(Y_1) \cos(Y_1) + Y_1 - \pi - \sin(Y_1) \cos(Y_1) \big)$.
These coefficients have the same structure as in the tensile case, only with Y_1 instead of Y_2 and they enter in (5.4) with an opposite sign.

Also, the solution $u_{n,c}$ from the perturbation method is similar to (5.23), only with a different $b_{n,c}$. In other words, the solution for the n-th harmonic amplitude due to the change in Young's modulus in the compressive case is

$$u_{n,c}(x,t) = \frac{\gamma_t b_{n,c} x}{n^2 k} \cos\big(n(\omega t - kx)\big). \tag{5.27}$$

The shift for compression leads to a similar structure of the Fourier coefficient as (5.24) and of the displacement field as (5.25).

5.3 Overall Solution and Simulation

Based on the previous section, the total solution u_2 from the perturbation method becomes

$$u_2(x,t) = A_{1,2}\sin\big(\omega t - kx + \tfrac{\pi}{2}\big) + A_{2,2}\sin\big(2(\omega t - kx + \tfrac{\pi}{2})\big) + A_{3,2}\sin\big(3(\omega t - kx + \tfrac{\pi}{2})\big) + \cdots, \tag{5.28}$$

where $A_{1,2}$ is the modification of the first harmonic amplitude due to the nonlinearity, $A_{2,2}$ is the second and $A_{2,3}$ is the third harmonic amplitude. The amplitudes read

$$A_{n,2} = \frac{x}{n^2 k}\big(- \gamma_t(b_{n,t} - b_{n,t,\text{shift}}) + \gamma_c(b_{n,c} - b_{n,c,\text{shift}})\big), \tag{5.29}$$

i.e. they are proportional to the propagation distance x and to the relative change in Young's modulus. Their dependency on the other parameters is indirect through the Fourier coefficients b_n.

Simulations show that $A_{1,2}$ is negative and proportional to the propagation distance. This fits the physical intuition that the amplitude of the first harmonic decreases because energy is transferred to the higher harmonics. To denote this difference, the initial first harmonic amplitude from the linear wave equation will be called $A_{1,1}$, and the modified first harmonic amplitude becomes $A_1' = A_{1,1} + A_{1,2}$.

It becomes clear in equation (5.29) that in the case of a trilinear stress-strain relationship

multiple effects generate acoustic nonlinearity: First, the relative change in Young's modulus on both the tensile and compressive side generates acoustic nonlinearity. The second reason is that the bilinear part of the stress-strain curve, resulting from the opening-closing motion, does not go through the origin due to rough surface contact in the intermediate region.

Figure 5.1 shows the contribution of these mechanisms. The amplitude A_2 resulting from tension, i.e. from the products in γ_t, is depicted by the dotted line, as a function of the initial first harmonic amplitude $A_{1,1}$. In a similar manner, the terms multiplied with γ_c lead to the second harmonic amplitude plotted as a dashed line. A propagating wave of sufficiently large amplitude leads to both opening and closing, so that A_2 is the sum of both effects, which is pictured as a solid line. The second harmonic amplitude is linearly related to $A_{1,1}$.

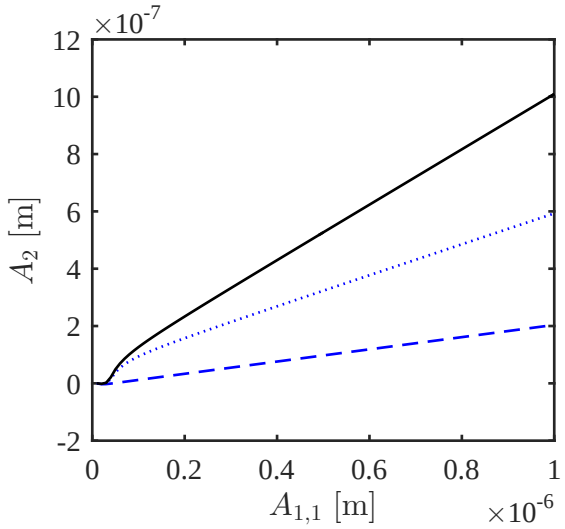

Figure 5.1: Second harmonic generation as a function of initial first harmonic amplitude. Mechanisms: 1. transition between asperity contact and open cracks (dotted), 2. transition between asperity contact and closed cracks (dashed), 3. both effects combined (solid line).

The solution u_2 also contains a third harmonic wave. Its amplitude is depicted in figure 5.2 by the dot dashed line. Unlike A_2, it does not increase with $A_{1,1}$, but the displacement amplitude remains approximately constant at $1 \cdot 10^{-8}$ m and is much smaller than the second harmonic amplitude.

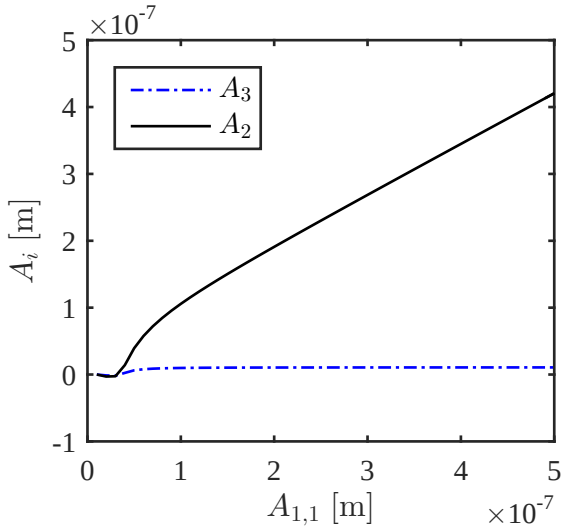

Figure 5.2: Second and third harmonic amplitudes as a function of initial first harmonic amplitude.

These results go beyond what has been calculated in the existing models by Zhao et al. [35] and Nazarov and Sutin [23] for multiple reasons.

First, the underlying model of the stress-strain relationship is advanced. It does not only contain one effect, but combines opening, closing and asperity contact of cracks.

Second, this leads to a more complex wave equation that accounts for multiple mechanisms that generate acoustic nonlinearity.

On the one hand, the literature on the RSC model focuses only on the nonlinearity β_{RSC} caused by the ε^2 term in the effective stress-strain relationship that results from the crack being in asperity contact. In the nonlinear wave equation which has been introduced in this chapter, however, also the transitions from asperity contact to completely open cracks under tension and to completely closed cracks under compression are included as a source of nonlinearity.

In their paper, Zhao et al. [35] calculate only the solution for the second harmonic wave and determine its amplitude. Applying a Fourier series expansion approach, as it is done in this thesis, shows that right-hand side of the perturbation equation from their derivation leads to only even harmonics. In the present work, however, all Fourier coefficients are

nonzero, so that even and odd harmonics are generated. In simulations, the amplitude of the third harmonic is much smaller than the one of the second harmonic, which matches physical intuition. Moreover, the derivation in this chapter shows that the nonlinearity also influences the first harmonic wave, leading to a decrease in the amplitude A_1, which agrees with the physical understanding.

Overall, this thesis develops a model that is more comprehensive than purely bilinear stiffness or RSC. Therefore, it describes the physical mechanisms that generate acoustic nonlinearity more accurately.

CHAPTER 6

EXPERIMENT

6.1 Experimental Procedure

The SHG technique using longitudinal waves is implemented as follows [30]: A generating transducer is attached to the specimen and sends a longitudinal sinusoidal wave of the fundamental frequency through the sample. While propagating, the wave interacts with the material's microstructure, as described in chapter 1. On the opposite side of the specimen, a second transducer receives the signal. The experimental setup is shown in figure 6.1.

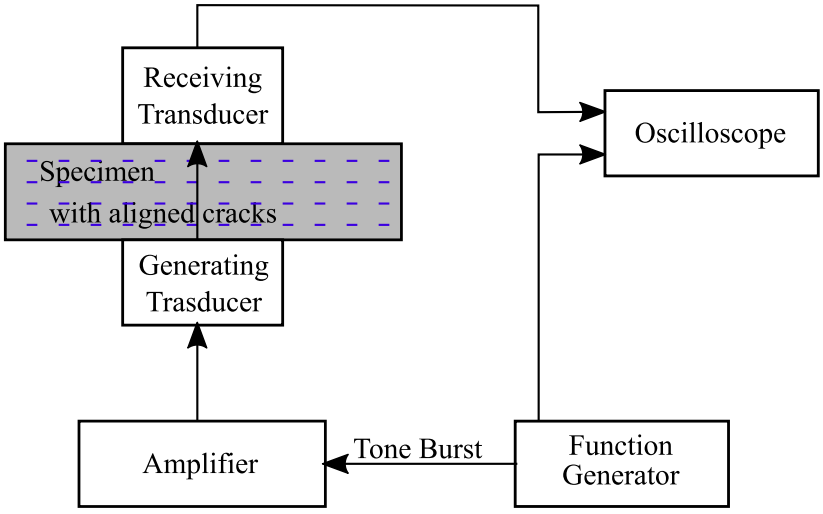

Figure 6.1: Schematic of the experimental setup, adapted from [30].

The fundamental signal has the frequency 5 MHz and is generated by a function generator as a tone burst of six cycles with burst period 20 ms. This signal is then transmitted to an amplifier and the amplified signal is the input to the transducer. The amplifier voltage is varied to generate waves of different amplitudes. The center frequency of the receiving piezoelectric transducer is 10 MHz, being twice the one of the 5 MHz generating transducer. This is specifically chosen for second harmonic measurements, where the

amplitudes of the second harmonic are much smaller than those of the fundamental. When attaching the transducers, a thin layer of oil is applied to enhance the coupling, and they are pressed to the material with a force distributed as evenly as possible. The signal from the receiving transducer is then transmitted to an oscilloscope, where it is recorded. In the next step, the recorded time-domain signals for the different input voltages are post-processed. In order to obtain the amplitudes of the fundamental wave and the second harmonic, the signal is processed with a known poles Prony method. Scott et al. [31] found that this method converges well even for a low number of cycles, because it uses the knowledge of the frequencies in the signal as a prediction.

In experiments, it is more practical to measure the voltage amplitudes of the first and second harmonics instead of the actual displacements. Recall that β (2.15) is defined as a relative parameter between the first and second harmonic amplitudes. The change in the absolute acoustic nonlinearity parameter is proportional to the relative change in β. By measuring the voltage, not only microstructural nonlinearities, but also system nonlinearities from, for instance, the transducer and the coupling are included. The system nonlinearities are proportional to the first harmonic squared [21], so that relative β measurements detect changes in the material nonlinearity.

6.2 Experimental Results

Figure 6.2a shows the measured voltage amplitude A_2 versus A_1. For small amplitudes A_1, the amplitude A_2 is a function of A_1^2 and the quadratic fit is plotted in blue. For high A_1 above 10 V, the increase in A_2 becomes smaller. A reason for this behavior could be saturation effects in the transducer. Measurements with this setup are usually made with $A_1 \leq 10$ V, where it was seen that these effects do not occur yet. For intermediate voltage amplitudes $4 \text{ V} \leq A_1 \leq 10$ V, both a quadratic and a linear fit with shift are plotted in figure 6.2a. Both fit the data well, so that the relationship in this interval lies in the range $A_2 \sim A_1^n$, $2 \geq n \geq 1$. For comparison, also the conventional definition (2.15) of β, where

$A_2 \sim A_1^2$, is applied in blue.

Figure 6.2b shows A_2 versus A_1^2 with a linear fit. The relative acoustic nonlinearity parameter β is then found by dividing the slope of the linear function by the thickness of the material, which yields $\beta = 3.413$. It is seen in the figure that the A_2 values for $60\ \mathrm{V}^2 \leq A_1 \leq 100\ \mathrm{V}^2$ are smaller than the linear fit, which indicates that possibly $A_2 \sim A_1^n$ with $n < 2$.

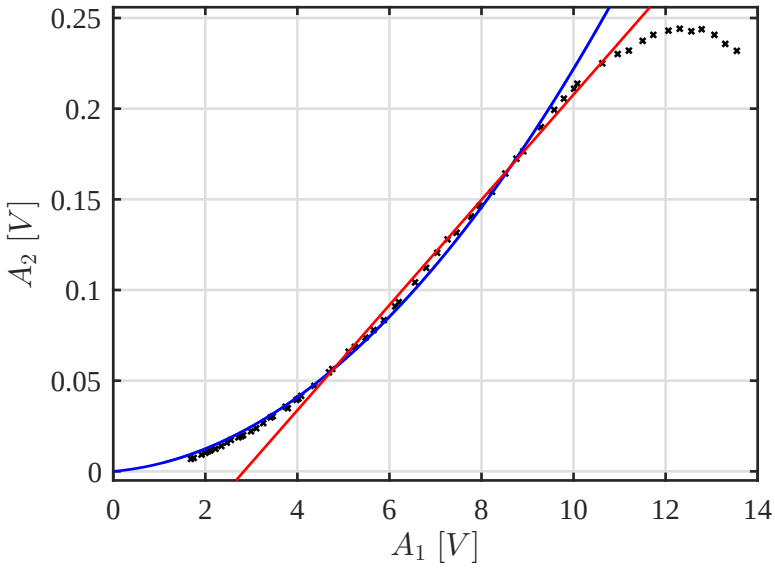

(a) A_2 vs. A_1 with linear and quadratic fit.

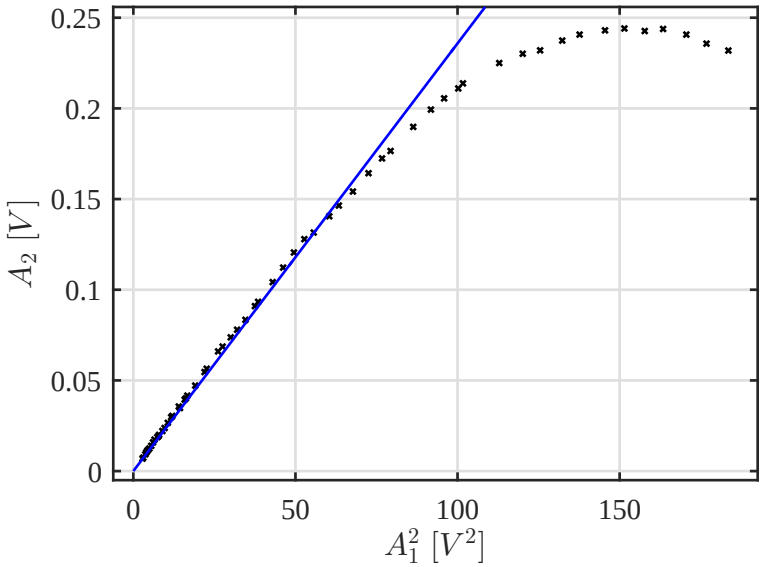

(b) A_2 vs. A_1^2 with $A_2 \sim A_1^2$ fit.

Figure 6.2: Measured voltage amplitudes and comparison of fits.

CHAPTER 7
CONCLUSION AND FUTURE WORK

7.1 Conclusion

This work consists of two major steps: An overall effective stress-strain relationship of a solid with aligned microcracks is developed, and a model for the nonlinear interactions between ultrasonic waves and microcracks is derived.

Depending on the strain state of the material, different effects dominate: The cracks are either open, in asperity contact or closed. The stress-strain relationship formulated in chapter 4 includes all of these effects. It is a combination of the bilinear stiffness model and the rough surface contact model. Physically, the transitions between the effects opening, closing and asperity contact are smooth, so that the overall stress-strain relationship and its derivative are continuous. The nonlinear model is the superposition of a trilinear part and a quadratic nonlinearity which can both be treated separately and correspond to two different mechanisms causing acoustic nonlinearity. Simulations have shown that the nonlinearity in the stress-strain relationship and, consequently, the acoustic nonlinearity increase with crack density and crack radius.

The interactions of aligned microcracks with a propagating longitudinal wave have been examined by inserting the overall nonlinear stress-strain relationship into the wave equation. The nonlinearity acts as a perturbation to the linear wave equation and a Fourier series expansion of this perturbation was carried out. In this series, all coefficients of the even and odd harmonics are nonzero. By solving the corresponding inhomogeneous PDEs, the respective amplitudes of the second, third, etc. harmonic wave were computed. The second harmonic amplitude is proportional to the propagation distance x. Beyond that, the simulations show that the amplitude of the first harmonic decreases proportionally to the

propagation distance, because energy is transferred to higher harmonics. For small amplitudes, the rough surface contact leads to the relationship $A_2 \sim A_1^2$. For larger amplitudes, when the opening-closing motion dominates, the amplitude A_2 of the second harmonic is linearly related to the fundamental amplitude A_1.

Experimental results from longitudinal wave measurements in the cracked NFA material confirm that for small amplitudes $A_2 \sim A_1^2$. For intermediate amplitudes, there is a smaller increase in A_2, so that approximately $A_2 \sim A_1$. For large amplitudes, however, $A_2(A_1)$ does not increase any further, which could either result from saturation effects in the measurements or from a mutual cancellation of effects that has not been derived in the current state of the model yet.

For different amplitude ranges, there exist different definitions of the acoustic nonlinearity parameter β in cracked solids, which cannot be combined. Therefore, describing the nonlinearity mathematically by β is not applicable, and it has to be quantified in terms of the amplitudes $A_2(A_1)$ instead.

7.2 Future Work

In this work, the computations of the overall stress-strain relationship and the amplitudes resulting from the wave equation have been performed in two separate steps. The next task in future work is to combine the calculations of both and to carry out parameter studies to further investigate the relationship between crack density, radius etc. and acoustic nonlinearity.

In the microcrack model incorporated in this thesis, multiple material parameters were estimated and assumed. In future work, these parameters, especially of the surface of the crack faces, could be determined experimentally.

Moreover, the transitions ε_1, ε_2 between the crack states have been calculated based on the physical argumentation of continuous and continuously differentiable stresses. In order to compare these values to the experiment, a relationship between the displacement

amplitude and the strain is required.

Since developing and testing NFA materials is a subject of current research, the characterization of their microstructure is not finalized yet. The acoustic nonlinearity observed in experiments may not only result from the microcracks, but also from other microstructural properties of the NFA, which have to be examined. Including additional effects would lead to a more and more comprehensive model for the effective properties of the material and the resulting acoustic nonlinearity generation.

REFERENCES

[1] J. Achenbach, *Wave propagation in elastic solids*. Elsevier, 2012, vol. 16.

[2] D. Broda, W. J. Staszewski, A. Martowicz, T. Uhl, and V. V. Silberschmidt, "Modelling of nonlinear crack–wave interactions for damage detection based on ultrasound – a review," *Journal of Sound and Vibration*, vol. 333, no. 4, pp. 1097–1118, 2014.

[3] S. R. Brown and C. H. Scholz, "Closure of random elastic surfaces in contact," *Journal of Geophysical Research: Solid Earth*, vol. 90, no. B7, pp. 5531–5545, 1985.

[4] O. Buck, W. L. Morris, and J. M. Richardson, "Acoustic harmonic generation at unbonded interfaces and fatigue cracks," *Applied Physics Letters*, vol. 33, no. 5, pp. 371–373, 1978.

[5] B. Budiansky and R. J. O'Connell, "Elastic moduli of a cracked solid," *International Journal of Solids and Structures*, vol. 12, no. 2, pp. 81–97, 1976.

[6] J. H. Cantrell, "Quantitative assessment of fatigue damage accumulation in wavy slip metals from acoustic harmonic generation," *Philosophical Magazine*, vol. 86, no. 11, pp. 1539–1554, 2006.

[7] J. H. Cantrell, "Acoustic nonlinearity from cracks," in *Ultrasonic nondestructive evaluation: Engineering and biological material characterization*, T. Kundu, Ed., CRC press, 2003, ch. 6.3.8, pp. 424 –429.

[8] J. H. Cantrell, "Ultrasonic harmonic generation," in *Ultrasonic nondestructive evaluation: Engineering and biological material characterization*, T. Kundu, Ed., CRC press, 2003, ch. 6.1.5, pp. 373 –375.

[9] J. H. Cantrell, "Crystalline structure and symmetry dependence of acoustic nonlinearity parameters," *Journal of Applied Physics*, vol. 76, no. 6, pp. 3372–3380, 1994.

[10] K. F. Graff, "Wave motion in elastic solids," 1991.

[11] J. A. Greenwood and J. B. P. Williamson, "Contact of nominally flat surfaces," *Proceedings of the Royal Society A*, vol. 295, no. 1442, pp. 300–319, 1966.

[12] R. A. Guyer and P. A. Johnson, "Nonlinear mesoscopic elasticity: Evidence for a new class of materials," *Physics Today*, vol. 52, pp. 30–36, 1999.

[13] H. Horii and S. Nemat-Nasser, "Overall moduli of solids with microcracks: Load-induced anisotropy," *Journal of the Mechanics and Physics of Solids*, vol. 31, no. 2, pp. 155–171, 1983.

[14] K. L. Johnson, *Contact mechanics*. Cambridge; New York: Cambridge University Press, 1985.

[15] M. L. Kachanov, "Effective elastic properties of cracked solids: Critical review of some basic concepts," *Applied Mechanics Reviews*, vol. 45, no. 8, pp. 304–335, 1992.

[16] M. L. Kachanov, "A microcrack model of rock inelasticity part I: Frictional sliding on microcracks," *Mechanics of Materials*, vol. 1, no. 1, pp. 19–27, 1982.

[17] J. H. Kim, T. S. Byun, D. T. Hoelzer, S.-W. Kim, and B. H. Lee, "Temperature dependence of strengthening mechanisms in the nanostructured ferritic alloy 14YWT: Part I – mechanical and microstructural observations," *Materials Science & Engineering A*, vol. 559, pp. 101–110, 2013.

[18] J.-Y. Kim, A. Baltazar, and S. I. Rokhlin, "Ultrasonic assessment of rough surface contact between solids from elastoplastic loading–unloading hysteresis cycle," *Journal of the Mechanics and Physics of Solids*, vol. 52, no. 8, pp. 1911–1934, 2004.

[19] J.-Y. Kim and J.-S. Lee, "A micromechanical model for nonlinear acoustic properties of interfaces between solids," *Journal of Applied Physics*, vol. 101, no. 4, p. 043 501, 2007.

[20] D. Krajcinovic, *Damage mechanics*. Elsevier, 1996.

[21] K. H. Matlack, J.-Y. Kim, L. J. Jacobs, and J. Qu, "Review of second harmonic generation measurement techniques for material state determination in metals," *Journal of Nondestructive Evaluation*, vol. 34, no. 1, p. 273, 2015.

[22] T. Mura, *Micromechanics of defects in solids*. The Hague: Martinus Nijhoff Publishers, 1982.

[23] V. E. Nazarov and A. M. Sutin, "Nonlinear elastic constants of solids with cracks," *The Journal of the Acoustical Society of America*, vol. 102, no. 6, pp. 3349–3354, 1997.

[24] T. Oberhardt, J.-Y. Kim, J. Qu, and L. J. Jacobs, "A contact mechanics based model for partially-closed randomly distributed surface microcracks and their effect on acoustic nonlinearity in rayleigh surface waves," in *AIP Conference Proceedings*, AIP Publishing, vol. 1706, 2016, p. 020 024.

[25] G. R. Odette, M. J. Alinger, and B. D. Wirth, "Recent developments in irradiation-resistant steels," *Annual Review of Materials Research*, vol. 38, pp. 471–503, 2008.

[26] G. R. Odette, "Recent progress in developing and qualifying nanostructured ferritic alloys for advanced fission and fusion applications," *The Journal of the Minerals, Metals & Materials Society*, vol. 66, no. 12, pp. 2427–2441, 2014.

[27] J. Qu and M. Cherkaoui, *Fundamentals of micromechanics of solids*. Hoboken, NJ: Wiley, 2006.

[28] J. M. Richardson, "Harmonic generation at an unbonded interface – I. planar interface between semi-infinite elastic media," *International Journal of Engineering Science*, vol. 17, no. 1, pp. 73–85, 1979.

[29] M. Rjelka, B. Köhler, and A. Mayer, "Nonlinear effects of micro-cracks on long-wavelength symmetric lamb waves," *Ultrasonics*, vol. 90, pp. 98–108, 2018.

[30] K. Scott, "Linear and nonlinear ultrasonic measurements on a transversely isotropic nanostructured ferritic (NFA) material to determine the sensitivity of these measurement techniques to changes in the microstructure," unpublished, 2017.

[31] K. Scott, J.-Y. Kim, and L. J. Jacobs, "Signal processing methods for second harmonic generation in thin specimens," *NDT & E International*, vol. 95, pp. 57–64, 2018.

[32] I. Solodov, D. Döring, and G. Busse, "New opportunities for NDT using non-linear interaction of elastic waves with defects," *Journal of Mechanical Engineering*, vol. 57, no. 3, pp. 169–182, 2011.

[33] I. Solodov, "Ultrasonics of non-linear contacts: Propagation, reflection and NDE-applications," *Ultrasonics*, vol. 36, no. 1-5, pp. 383–390, 1998.

[34] S. Timoshenko and J. Goodier, *Theory of elasticity*. McGraw-Hill, 1951.

[35] Y. Zhao, Y. Qiu, L. J. Jacobs, and J. Qu, "A micromechanics model for the acoustic nonlinearity parameter in solids with distributed microcracks," in *AIP Conference Proceedings*, AIP Publishing, vol. 1706, 2016, p. 060 001.

[36] Y. Zhao, Y. Qiu, L. J. Jacobs, and J. Qu, "Frequency-dependent tensile and compressive effective moduli of elastic solids with distributed penny-shaped microcracks," *Acta Mechanica*, vol. 227, no. 2, pp. 399–419, 2016.